The role of bottom friction in mediating the response of the Weddell Gyre circulation to changes in surface stress and buoyancy fluxes

Julia Neme [a,b] , Matthew H. England,[b,c] , Andrew McC. Hogg [d] ,
Hemant Khatri [e,f] , Stephen M. Griffies [f,g]

[a] *Climate Change Research Centre and ARC Centre of Excellence for Climate Extremes, University of New South Wales, Sydney, Australia*

[b] *Australian Centre for Excellence in Antarctic Science, University of New South Wales, Sydney, Australia*

[c] *Centre of Marine Science and Innovation, Evolution and Ecology Research Centre, School of Biological, Earth and Environmental Sciences, University of New South Wales, Sydney, Australia*

[d] *Research School of Earth Sciences and ARC Centre of Excellence for Climate Extremes, Australian National University, Canberra, Australia*

[e] *Department of Earth, Ocean and Ecological Sciences, School of Environmental Sciences, University of Liverpool, Liverpool, UK*

[f] *Princeton University Atmospheric and Oceanic Sciences Program, Princeton NJ, USA*

[g] *NOAA Geophysical Fluid Dynamics Laboratory, Princeton, NJ, USA*

Corresponding author: Julia Neme, j.neme@unsw.edu.au

ABSTRACT: The Weddell Gyre is one of the dominant features of the Southern Ocean circulation and its dynamics have been linked to processes of climatic relevance. Variability in the strength of the gyre's horizontal transport has been linked to heat transport towards the Antarctic margins and changes in the properties and rates of export of bottom waters from the Weddell Sea region to the abyssal global ocean. However, the precise physical mechanisms that force variability in the Weddell's lateral circulation across different timescales remain unknown. In this study, we use a barotropic vorticity budget from a high-resolution model simulation to attribute changes in gyre strength to variability in possible driving processes. We find that the Weddell Gyre's circulation is sensitive to bottom friction associated with the overflowing dense waters at its western boundary. In particular, an increase in the production of dense waters at the southwestern continental shelf strengthens the bottom flow at the gyre's western boundary, yet this drives a weakening of the depth-integrated barotropic circulation via increased bottom friction. Strengthening surface winds initially accelerates the gyre, but within a few years the response reverses once dense water production and export increases. These results reveal that the gyre can weaken in response to stronger surface winds, putting into question the traditional assumption of a direct relationship between surface stress and gyre strength in regions where overflowing dense water forms part of the depth-integrated flow.

1. Introduction

a. The Weddell Gyre

The Weddell Gyre (Figure 1), located in the Southern Ocean south of the Antarctic Circumpolar Current (ACC), is a dynamically complex region that sets the scene for a variety of processes that influence the global climate (Vernet et al. 2019). The gyre's horizontal circulation acts as a buffer, separating the relatively warm waters of the ACC from the colder continental margin. This mediating role is particularly important in the context of heat transport towards the ice shelves (Narayanan et al. 2023; Naveira Garabato et al. 2016; Wilson et al. 2022), as well as bottom water formation and export, a process that sequesters atmospheric carbon to store it in the abyssal ocean (Meredith 2013; Purkey et al. 2018). Moreover, the Weddell Gyre's circulation has been linked to polynya occurrence (Zhou et al. 2022) as well as sea ice formation and advection (Morioka and Behera 2021). However, despite its influential role in regional and global processes, the dynamics and drivers of variability of the Weddell Gyre's circulation remain poorly understood.

One of the few locations of Dense Shelf Water (DSW) production around the Antarctic margins is at the southwestern continental shelf in the proximity of the Filchner Ronne-Ice Shelf, both within ice shelf cavities and open ocean. DSW is a precursor of Antarctic Bottom Water (AABW) that is formed from water masses that have been advected within the Weddell Gyre's circulation (Foster and Carmack 1976; Narayanan et al. 2019). A fraction of the DSW formed in the continental shelf overflows into the Weddell Gyre, becomes entrained with ambient waters and follows the gyre's circulation northwards (Solodoch et al. 2022). Whilst the densest portion of these waters remain within the gyre, a lighter fraction is able to escape via narrow passages into the Scotia Sea to fill the global abyssal ocean (e.g., Naveira Garabato et al. 2019) and is hereafter referred to as AABW. The rates and properties of AABW export to the global ocean have been suggested to be partly determined by the Weddell Gyre itself, with changes in its volume, temperature and salinity linked to changes in the strength of the gyre's horizontal transport (Gordon et al. 2010; Meredith et al. 2011; Meijers et al. 2016; Gordon et al. 2020). The exact mechanism by which gyre strength is linked to export is not yet fully understood, with different arguments proposing wind-driven changes to the baroclinicity of the gyre (Meredith et al. 2008), barotropic accelerations of its boundary currents (Meredith et al. 2011; Meijers et al. 2016) and changes in production or export from the continental shelf (Abrahamsen et al. 2019).

Unlike other ocean gyres, the Weddell lacks topographic constraints to the east, allowing for an open eastern boundary (Figure 1a). The eastern boundary is a dynamic feature, located generally between 30°E and 50°E and allows for zonal expansions/contractions of the gyre's area across different time scales (Neme et al. 2021), as well as for significant import of different water masses into the region via instabilities and the mean flow (Leach et al. 2011; Ryan et al. 2016). For example, Circumpolar Deep Water (CDW) enters through the east and flows westward along the southern limb of the Weddell Gyre, identifiable in temperature observations (Reeve et al. 2019). CDW is transformed by mixing and upwelling within the Weddell Gyre and becomes an important source of salinity for DSW formation (Nicholls et al. 2009). Both observations and model simulations suggest that AABW also enters the region through the east, flowing westwards to join the bottom waters overflowing the continental shelf in the vicinity of the Filchner-Ronne Ice Shelf (Couldrey et al. 2013; Jullion et al. 2014; Solodoch et al. 2022).

The relation between Weddell Gyre strength and surface stress as a driving mechanism remains elusive, in particular in connection to forced changes to gyre circulation (Neme et al. 2021; Auger et al. 2022). One of the specific challenges in the region is the extensive presence of sea ice, which substantially modifies the transfer of momentum at the ocean's surface (Dotto et al. 2018; Naveira Garabato et al. 2019). Sea ice changes also lead to intense surface buoyancy fluxes, which have been shown to be capable of setting a gyre circulation (Hogg and Gayen 2020) and influence gyre strength (Wang and Meredith 2008). An additional complexity to the dynamics of the gyre is the inclusion of the Antarctic Slope Current (ASC) at the southern and western boundaries (see Thompson et al. 2018, for a review). The ASC is a quasi-circumpolar feature of the Antarctic margin's ocean circulation and is subject to its own dynamics, which have been suggested to influence the circulation of the gyre itself (Le Paih et al. 2020). Fahrbach et al. (2011) even suggest that the northern and southern limb of the Weddell Gyre can vary independently in response to different forcings.

In light of the influence of the Weddell Gyre's circulation on regional and global processes, it is important to identify the mechanisms that force changes to the gyre's circulation. In particular, we are interested in determining the adjustment processes behind the gyre's response to changes

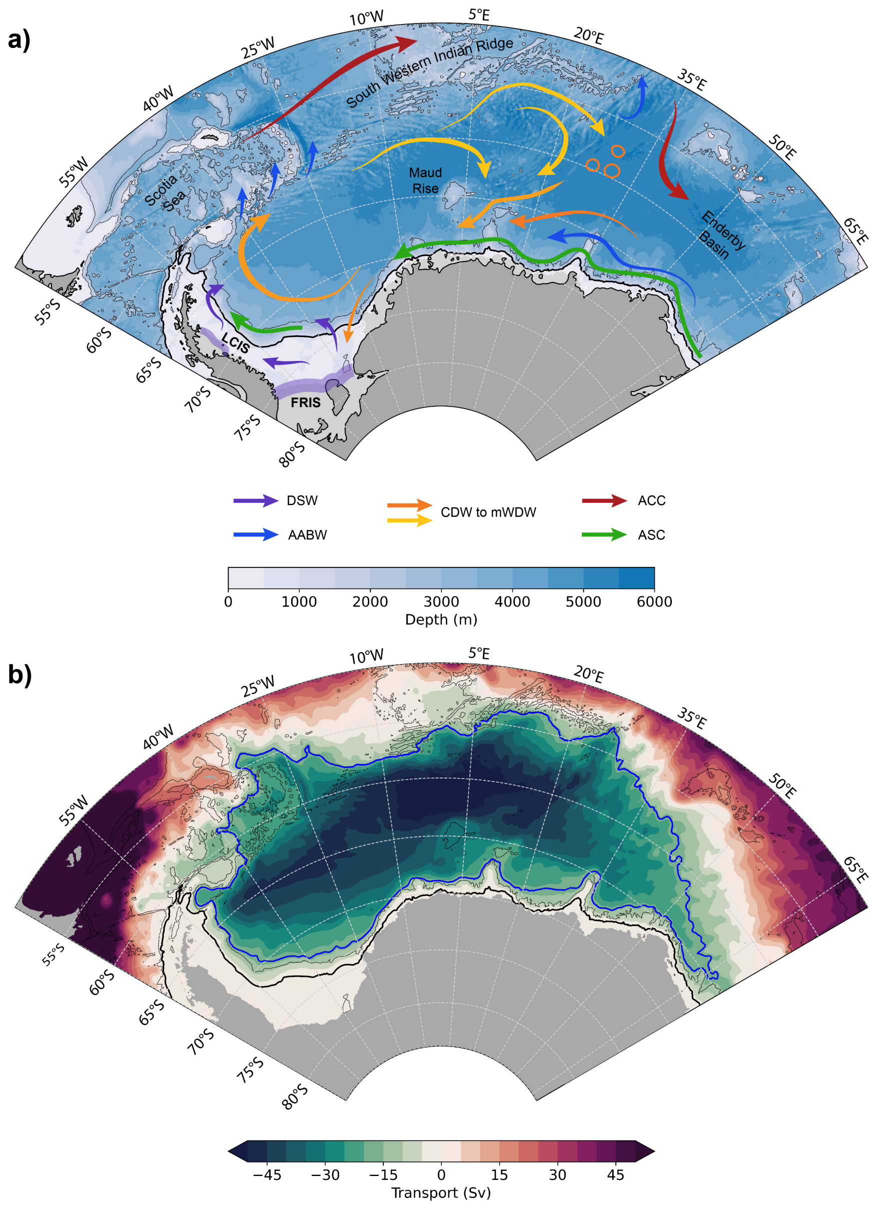

FIG. 1. **a)** Schematic of the main circulation pathways, key water masses and topographic features of the Weddell Gyre region. DSW = Dense Shelf Water, AABW = Antarctic Bottom Water, CDW = Circumpolar Deep Water, mWDW = modified Warm Deep Water, ACC = Antarctic Circumpolar Current, ASC = Antarctic Slope Current, FRIS = Filchner-Ronne Ice Shelf, LCIS = Larsen C Ice Shelf. Black thick contour shows the 1000m isobath that follows the continental slope. **b)** Mean barotropic streamfunction for our control simulation (1 Sv = 10^6 m^3 s^{-1}) with -17 Sv contour in blue.

in possible forcings. We do so by analysing the barotropic vorticity budget of the Weddell Gyre, which is introduced in the following section.

b. The barotropic vorticity budget in theories of gyre circulation

A comprehensive study of the mechanisms that set the strength of the Weddell Gyre needs to take into account the complex dynamics mentioned above. A useful dynamical framework from which to address this question is the barotropic vorticity budget (hereafter referred to as BVB). The BVB is derived from the momentum equations and can be used to determine what physical mechanisms act as a source or sink of vorticity in a system. Textbook theories of gyre circulation are derived from the vorticity balance under different assumptions. In one of the earliest solutions to the BVB, Sverdrup (1947) assumes an inviscid, flat-bottomed ocean in a steady state away from the western boundary, and recovers a mean state in which the input of vorticity by the wind is balanced by meridional flow in the interior of the ocean. Subsequent theories looking to include western boundary currents propose lateral or bottom friction, maintaining the flat-bottomed ocean assumption (Stommel 1948; Munk 1950). An alternative solution proposed by Hughes (2000) that does not rely on friction, shows that it is possible to achieve a closure of the circulation by allowing a sloping wall at the western boundary. The wall, representing the continental slope, gives rise to a new term in the vorticity balance called the bottom pressure torque (hereafter BPT) (Holland 1973). When integrated over latitude lines, the BPT balances the input of vorticity by the wind in the ocean interior.

Numerical models allow calculation of the BVB without the need for assumptions such as an inviscid or a flat-bottom ocean, making the budget a very useful diagnostic tool of the ocean circulation. Hughes and De Cuevas (2001) use a numerical model to show that the BPT balances the wind stress curl when integrated over zonal strips, confirming the Hughes (2000) argument. While similar works show that the BPT-wind stress curl balance applies to the circulation of the North Atlantic subtropical gyre (Yeager 2015; Schoonover et al. 2016), balances involving other terms of the BVB dominate in other regions of the ocean (Sonnewald et al. 2019, 2023). In particular, at high latitudes the influence of bottom friction, horizontal viscosity and nonlinear effects becomes comparable to those of the bottom pressure torque and surface stress curl. Using an eddy-resolving model, Le Corre et al. (2020) find that the interior of the subpolar gyre in the

North Atlantic is forced by the nonlinear terms, which advect vorticity from the boundary into the interior, where it is balanced by the bottom drag curl.

In this work, we apply the barotropic vorticity budget framework in a high resolution ocean-sea ice model in order to identify the physical mechanisms that determine the strength of the Weddell Gyre's horizontal circulation. Our aim is to clarify the processes that force variability in gyre strength, and study the adjustments to the circulation following a perturbation in these forcings. Section 2 details the model used and Section 3 the barotropic vorticity budget framework. In Section 4 we describe our results and in Section 5 we summarize our main findings and discuss implications and caveats. Section 6 presents the conclusions of this study.

2. The Ocean Sea-ice Model

This study uses a Southern Ocean regional configuration (PanAntarctic) of a coupled ocean/sea ice model. The ocean component is version 6 of the Modular Ocean Model (MOM6) coupled with version 2 of the Sea Ice Simulator (SIS2), developed by the Geophysical Fluid Dynamics Laboratory (Adcroft et al. 2019; Griffies et al. 2020). The horizontal grid spacing of our PanAntarctic model is 0.1°, which admits mesoscale eddies in our study region, but fails to fully resolve their features given that the Rossby radius of deformation is less than 10 km (Hallberg 2013). For the vertical we make use of 75 vertical layers with a z^* vertical coordinate (Adcroft and Campin 2004). The stress at the ocean associated with bottom drag is quadratic, with a constant, non-dimensional bottom drag coefficient of 0.003. In the horizontal, MOM6 uses Laplacian viscosity with Smagorinsky biharmonic viscosity following Griffies and Hallberg (2000).

Our control simulation is forced at the surface with a prescribed atmosphere from JRA55-do version 1.4 (Tsujino et al. 2018) in a repeat year forcing configuration in which a 12-month period (from May 1990 to April 1991) is cycled continuously. This 12-month period was chosen due to the neutral state of several climate indices (e.g. El Niño-Southern Oscillation, Southern Annular Mode; for more details see Stewart et al. 2020). Part of the forcing data set from JRA55-do is runoff, which includes Antarctic calving and basal melt estimates from Depoorter et al. (2013). Freshwater is applied at the surface, constant in time but with varying spatial distribution, amounting to a total volume flux of 0.0847 Sv circumpolarly. The PanAntarctic model has an open northern boundary condition located at 37°S that comes from daily temperature, salinity and velocity fields from a global simulation of the Australian Community Climate and Earth System Simulator (ACCESS-OM2) (Kiss et al. 2020), which is forced with the same prescribed atmospheric state as the PanAntarctic simulation.

After 35 years of spin up of the control simulation (CTRL), we carry out six different perturbation experiments. One set of perturbations doubles and halves the bottom friction coefficient (DRAG2x and DRAG0.5x respectively). A second set decreases and increases DSW formation rates by locally adding or removing 50% of meltwater (MW+ and MW- respectively). Note that in all experiments, this meltwater is applied at the surface as a runoff term, since the model has no resolved ice shelf cavities or iceberg redistribution. We apply the perturbation circumpolarly, without altering the spatial distribution of freshwater input in CTRL. For a final set of experiments, we increase and decrease surface wind speed by 10% (WIND+ and WIND- respectively) over the entire model domain for both the meridional and zonal components of the wind.

3. Barotropic vorticity budget

We obtain the BVB by depth-integrating the horizontal momentum equations and subsequently applying the curl operator. The complete steps are detailed in Appendix A, as developed in Khatri et al. (2023), and the resulting BVB is:

$$\begin{aligned}\underbrace{\beta V}_{\text{Planetary vorticity advection}} = & \underbrace{\frac{J(p_b,H)}{\rho_0}}_{\text{Bottom pressure torque}} - \underbrace{\frac{fQ_m}{\rho_0}}_{\text{Surface mass flux}} + \underbrace{f\partial_t\eta}_{\text{Sea level tendency}} - \underbrace{\hat{\boldsymbol{z}}\cdot\nabla\times\mathcal{U}_t}_{\text{Rel. vorticity tendency}} \\ & + \underbrace{\frac{\hat{\boldsymbol{z}}\cdot\nabla\times\tau_{\mathbf{s}}}{\rho_0}}_{\text{Surface stress curl}} - \underbrace{\frac{\hat{\boldsymbol{z}}\cdot\nabla\times\tau_{\mathbf{b}}}{\rho_0}}_{\text{Bottom drag curl}} + \underbrace{\hat{\boldsymbol{z}}\cdot\nabla\times\mathcal{A}}_{\text{Nonlinear terms}} + \underbrace{\hat{\boldsymbol{z}}\cdot\nabla\times\mathcal{B}}_{\text{Horizontal viscosity}}\end{aligned} \tag{1}$$

where $\beta = \partial_y f$ is the meridional derivative of the Coriolis parameter and V is the depth-integrated meridional velocity. The bottom pressure torque is contained in $J(p_b, H)$, which is the Jacobian between bottom pressure, p_b, and bottom topography, H. Q_m is the mass flux across the ocean's surface, η is the free surface, and τ_s and τ_b are surface and bottom frictional stresses, respectively, with $\rho_0 = 1035\ kg\ m^{-3}$ the Boussinesq reference density. Surface stress takes into account the relative contributions of the air/ocean and sea ice/ocean stresses weighted by sea ice concentration.

$\mathcal{U}_t$ is the vertically integrated velocity tendency and $\mathcal{A}$ and $\mathcal{B}$ are the vertically integrated nonlinear advection and horizontal viscosity terms, respectively. There is an alternative approach to calculate the BVB that performs a depth-averaging rather than a depth-integration of the momentum equations. Using the depth-averaged flow yields another version of the BVB that contains the JEBAR term (joint effect of baroclinicity and relief) which has been shown to misinterpret the interaction with the topography (Mertz and Wright 1992; Cane et al. 1998). We therefore choose the depth-integrated approach.

MOM6 uses an Arakawa C-grid, which has been shown to produce spurious bottom pressure torques in the vorticity budget originating from the Coriolis force and the representation of topography (Styles et al. 2022; Waldman and Giordani 2023). We employ the method developed in Khatri et al. (2023), which diagnoses the bottom pressure torque in a way that handles the numerical errors associated with the C-grid, rendering a physically sensible diagnostic (see Appendix B in Khatri et al. (2023)).

The terms in Equation (1) balance at all locations, and hence can be integrated spatially to determine the dominant terms associated with the barotropic vorticity. Different balances are established in different regions of the ocean (e.g., Sonnewald et al. 2019; Le Corre et al. 2020; Sonnewald et al. 2023) and results are highly dependent on how the integration boundaries are chosen. Stewart et al. (2021) study how different definitions of gyre boundary can impact the magnitude of the different terms in the integrated BVB. They find that integrating over latitude bands yields a dominating bottom pressure torque balancing surface stress (as in Hughes (2000) and Hughes and De Cuevas (2001)), whilst integrating within a given barotropic streamfunction contour highlights the importance of other terms in the budget such as bottom friction. Since the focus of this study is the dynamics of the Weddell Gyre, we choose to integrate the BVB within a barotropic streamfunction contour.

The large-scale and low frequency depth-integrated circulation is nearly non-divergent, in which case the barotropic streamfunction (Figure 1b), $\boldsymbol{U} = -\hat{\boldsymbol{z}} \times \nabla\psi$, can be diagnosed by

$$\psi(x,y) = \rho_0^{-1} \int_{y_0}^{y} U(x,y')dy' = \rho_0^{-1} \int_{y_0}^{y} \int_{-H}^{\eta} u(x,y',z)\,\mathrm{d}z\,\mathrm{d}y', \tag{2}$$

where U is the vertically integrated zonal velocity, $z = -H(x,y)$ is the ocean bottom, $z = \eta(x,y,t)$ is the free surface, and the southern boundary for the integration, y_0, is taken at the Antarctic coastline. Given the above calculation, the streamfunction has negative values for the cyclonic Weddell Gyre (see Figure 1b). Note that this definition of streamfunction is of the opposite sign to the more general OMIP approach (Griffies et al. 2016), but is the one used in past studies of the Weddell Gyre (Vernet et al. 2019; Neme et al. 2021).

The integration ($\mathcal{I}$) of a term of the BVB budget (Ω) within the gyre's area, A, is

$$\mathcal{I}(t) = \int_A \Omega(t)\ dA. \tag{3}$$

We are interested in the time-evolution of Ω, as illustrated by the change of $\mathcal{I}$. Therefore, we choose a time-invariant area of integration, A, so that:

$$\partial_t \mathcal{I}(t) = \int_A \partial_t \Omega(t)\ dA \tag{4}$$

where A is defined using the -17 Sv contour from the barotropic streamfunction of the time-average of the CTRL simulation after spin-up (Figure 1b), which is the largest closed contour of circulation and represents the interior of the Weddell Gyre. We maintain the same area of integration across model simulations to facilitate the comparison between CTRL and the perturbation experiments.

When calculating the BVB in Equation (1), the planetary vorticity advection, surface mass flux and sea level tendency terms are derived from $\nabla \cdot (f\boldsymbol{U})$ (see Appendix A). Using the divergence theorem, we can write the area integral of a divergence, in this case $\nabla \cdot (f\boldsymbol{U})$, as the flux of the corresponding vector field integrated along the boundary, such that:

$$\begin{aligned} \int_A \nabla \cdot (f\boldsymbol{U})\ dA &= \int_{S_\psi} f\boldsymbol{U} \cdot \hat{\boldsymbol{n}}\ dS_\psi \\ &= \int_A (\beta V + f\frac{Q_m}{\rho_0} + f\partial_t \eta)\ dA \end{aligned} \tag{5}$$

Upon integration within a closed streamline, $\int_{S_\psi} f\boldsymbol{U} \cdot \hat{\boldsymbol{n}}\ dS_\psi = 0$, and if the surface mass flux and sea level tendency terms are also small, then $\int_A \beta V\ dA \approx 0$. We verify that indeed, the contributions of fQ_m/ρ_0 and $f\partial_t\eta$ are negligible in our simulations (see Figures 3, 4) so that $\nabla \cdot (f\boldsymbol{U}) \approx \beta V$ and we expect its integration within the -17 Sv contour to be zero for the time mean of our CTRL simulation used to define the area A. In the perturbation experiments, small expansions, contractions or displacements of the -17 Sv contour will yield a non-zero βV integration. In addition to the Weddell Gyre interior, we define a coastal boundary region using the 1000m isobath as its shoreward limit, and the -17 Sv contour of the Weddell Gyre boundary as its offshore limit. We refer to the western boundary as the portion west of 25°W of the coastal boundary. These areas are depicted in Figure 4a.

4. Results

In the following sections we describe the time-mean vorticity balance of the CTRL simulation post spin-up (years 35 to 50 in Figure 2) and follow with the response of the barotropic vorticity balance in the perturbation experiments that change the bottom drag coefficient (DRAG0.5x and DRAG2x), meltwater input (MW- and MW+) and surface wind speeds (WIND- and WIND+) in connection with the changes to gyre strength. We finalize with an analysis of the increase in gyre strength during the spin-up period of our CTRL simulation, aided by the insight gained with the perturbation experiments.

a. Control simulation

We define gyre strength as the absolute value of the minimum of ψ, which represents the total transport between the Antarctic continent and the center of the gyre. During the spin-up of our CTRL simulation, gyre strength increases from an initial value of 35 Sv to roughly 50 Sv average transport after 35 years (Figure 2).

We calculate the time-mean BVB terms from Equation (1) for the CTRL simulation after spin-up, shown in Figure 3, and check budget closure by computing the sum of the terms on the RHS of Equation (1) and verifying that the residual with respect to βV is of the order of the machine precision error (not shown). The maps in Figure 3 allow for the identification of areas of significance for each of the terms. Since the Weddell Gyre has a cyclonic (clockwise) circulation structure, negative values in the BVB terms represent sources of cyclonic vorticity while positive values represent sinks. Surface stress curl ($\hat{z} \cdot \nabla \times \tau_s$, Figure 3d) is the only term that ubiquitously acts as a source of cyclonic vorticity throughout the gyre's extent, while the rest of the terms display large spatial variability in their role as source/sink. The advection of planetary vorticity (βV, Figure 3a), roughly shows the northward flow confined to the western region of the gyre and the southward return flow to the east. The frictional terms, both with the bottom ($-\hat{z} \cdot \nabla \times \tau_b$, Figure

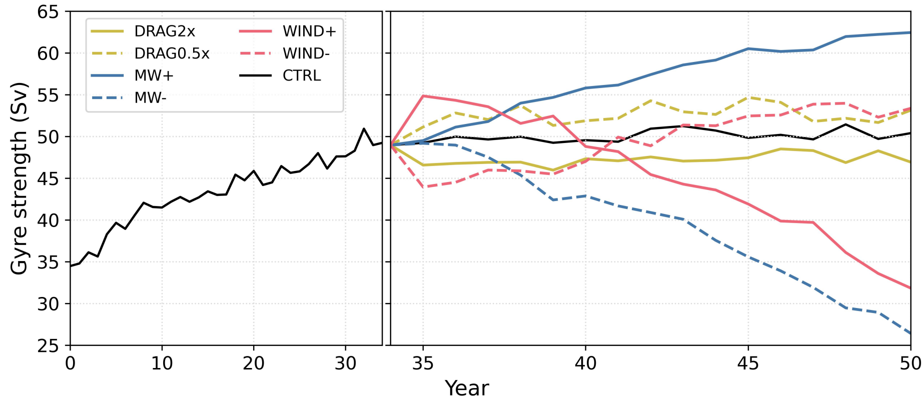

FIG. 2. Gyre strength (annual mean), calculated as the absolute value of the minimum of the barotropic streamfunction (Sv; 1 Sv = 10^6 m^3 sec^{-1}), for the control (CTRL) simulation (black) during the spin-up period (left panel, years 0 to 34) and for all simulations after the spin-up period (right panel, years 34 to 50). DRAG0.5X and DRAG2x represent the halved and doubled bottom drag coefficient experiments, MW- and MW+ the 50% reduction and increase in meltwater input experiments and WIND- and WIND+ the 10% reduction and increase in surface winds experiments respectively.

3e) and horizontal viscosity ($\hat{z}\cdot\nabla\times\mathcal{B}$, Figure 3g), display the largest magnitudes at the continental slope and other regions with large topographic gradients, such as South-West Indian Ridge.

The bottom pressure torque (BPT, Figure 3i) and the nonlinear advection term ($\hat{z}\cdot\nabla\times\mathcal{A}$, Figure 3f) display large spatial variability and small scale features several orders of magnitude larger than any of the other terms. Their sum (Figure 3b) resembles the βV term, consistent with the results of Le Corre et al. (2020) for the North Atlantic subpolar gyre. This resemblance increases with the size of the spatial filter due to the impact of filtering on the nonlinear advection terms, consistent with Hughes (2000) and Hughes and De Cuevas (2001), and explored in detail in Khatri et al. (2023). A sufficiently large filter length scale yields a balance resembling that of the coarse model of Yeager (2015), in which the BPT balances planetary vorticity advection. Khatri et al. (2023) provide a scaling argument, wherein the higher order derivatives included in the nonlinear advection term can only be compensated by those within the BPT term. Therefore, at small spatial scales characteristic of transient eddies and meanders, the meridional circulation is controlled primarily by the nonlinear advection terms and BPT (i.e. $\beta V \approx BPT + \hat{z}\cdot\nabla\times\mathcal{A}$). The residual from these two terms induces large-scale meridional motion in βV.

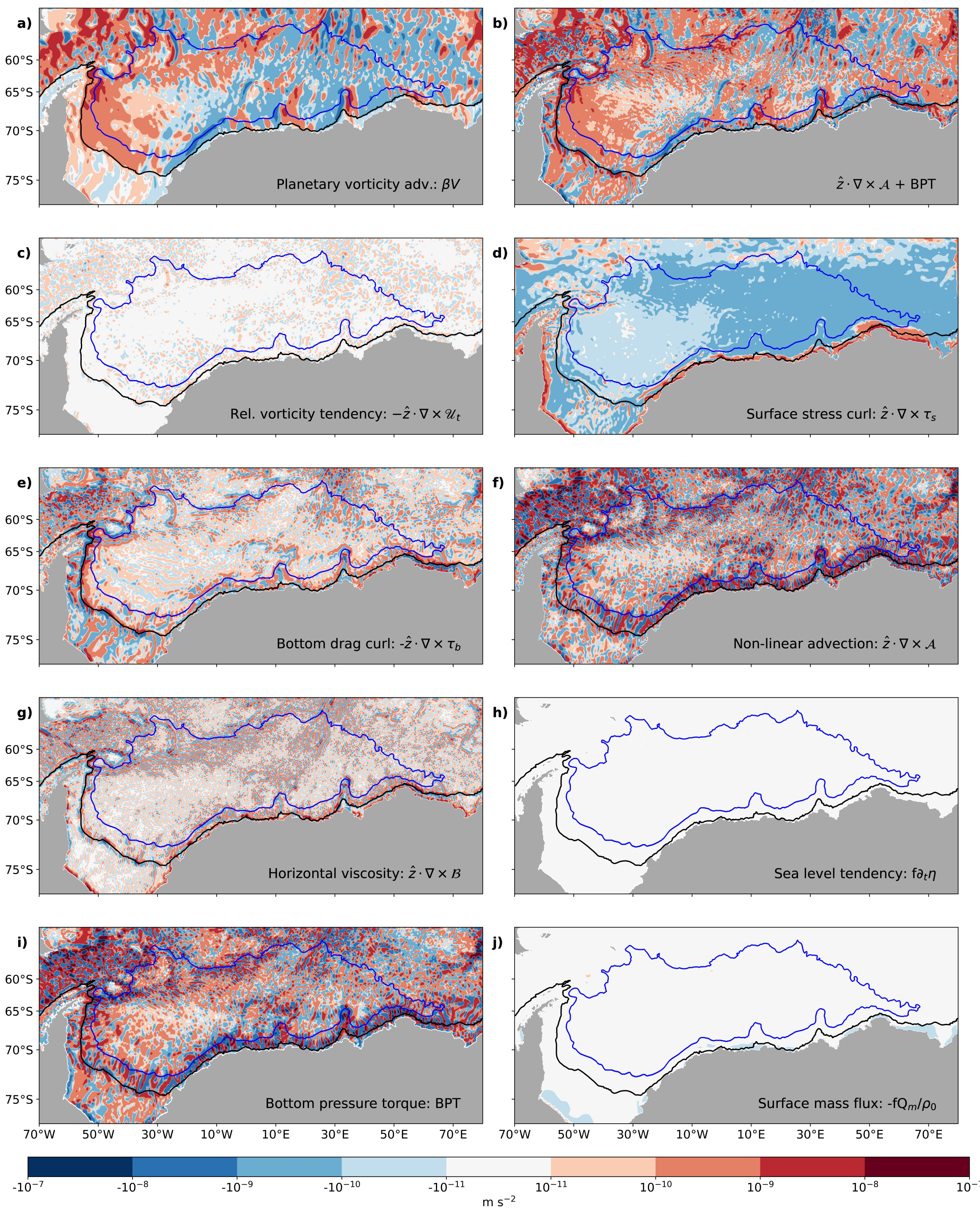

FIG. 3. Time-averaged maps of the terms in the BVB (Eq. 1) for the control simulation after spin-up (years 34 to 50), and the sum of the nonlinear term ($\hat{z}\cdot\nabla\times\mathcal{A}$) plus the BPT term. Negative (blue) values are adding cyclonic (clockwise) vorticity to the gyre and positive (red) values remove it. Black contour shows the 1000m isobath and blue contour the Weddell Gyre's boundary defined as the -17 Sv contour of the barotropic streamfunction. All fields have been smoothed using a 1° Gaussian filter from Grooms et al. (2021) and Loose et al. (2022).

The rate of change of relative vorticity ($-\hat{z}\cdot\nabla\times\mathcal{U}_t$, Figure 3c), sea level tendency ($f\partial_t\eta$, Figure 3h) and surface mass flux ($-fQ_m/\rho_0$, Figure 3j) terms are locally small. These terms do not play a significant role in the overall budget; therefore, we exclude them from the subsequent analysis.

The maps in Figure 3 are useful to identify areas of importance, but because of the high spatial variability and varying orders of magnitude it is difficult to quantify which terms are involved in the overall balance of the Weddell Gyre. Therefore, we integrate the terms in the budget, following Equation 3, within three regions shown in Figure 4a. Note that the integration is performed on the raw model output prior to any spatial filtering. The blue region depicts our definition of the Weddell Gyre interior using the -17 Sv contour. Additionally, we integrate over a coastal boundary between the 1000m isobath and the gyre's boundary (shown in pink) and a western subset of the coastal boundary (in pink and hatching). Even though the coastal boundary thus defined is not included within our definition of the Weddell Gyre interior, our calculation of the streamfunction implies that the transport at the coastal boundary is included within the gyre strength (since the Antarctic continent is the southern limit of integration in Equation (2)). This coastal boundary region includes the Weddell's boundary current system and the ASC.

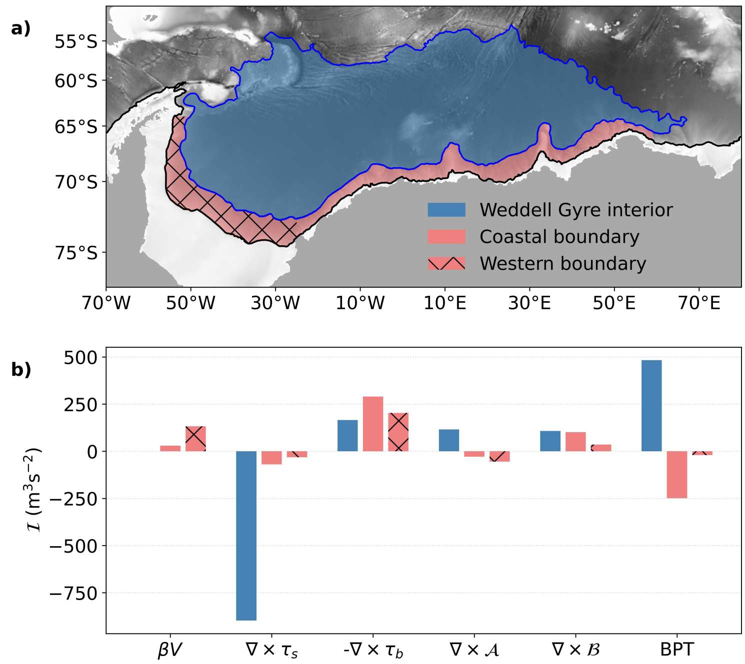

FIG. 4. **a)** Schematic of the areas of integration, with the Weddell Gyre interior defined by the -17 Sv contour of the barotropic streamfunction (light blue), the coastal region comprised between the 1000m isobath and the interior (pink), and a subset of the coastal region west of 25°W that represents the western boundary region (hatched pink). **b)** Integrated terms of the BVB of Equation (1) from the control simulation within each of the regions in **a**). As in Figure 3, negative values represent sources of cyclonic (clockwise) vorticity and positive are sinks. The surface mass flux ($-fQ_m/\rho_0$), sea level tendency ($f\partial_t\eta$) and relative vorticity tendency ($-\hat{z}\cdot\nabla\times\mathcal{U}_t$) are excluded from **b)** because they are negligible in the main vorticity balance. Also, note that $\int \beta V \, \mathrm{d}A \approx 0$ for the Weddell Gyre interior region given that it is defined by a mean streamline.

The integration $\mathcal{I}$ of the terms in the BVB for the time-average of the CTRL simulation is shown in Figure 4b for the regions marked in Figure 4a. Within the gyre interior the only source of cyclonic vorticity is the surface stress curl term, which is balanced primarily by the interactions with topography associated mainly with the BPT and smaller contributions from the bottom drag curl. The nonlinear and horizontal viscosity terms play a secondary role as sinks of cyclonic vorticity. The rest of the terms in Equation (1) are not significant in the mean balance. Particularly, when integrated within a closed streamline the planetary advection term vanishes for the reasons outlined in Section 3. The role of bottom friction as a sink of cyclonic vorticity gains importance at the coastal boundary, especially in the western region. This result is to be expected due to the proximity of the continental slope and the presence of the bottom-intensified ASC regime that characterises regions with DSW overflow (Huneke et al. 2022) and is therefore subject to larger bottom drag.

The following sections focus on the response of gyre strength to different perturbations designed to explore forced changes in the gyre's horizontal transport. We focus on the time-varying terms integrated within the Weddell Gyre area rather than on a time-averaged state.

b. Role of bottom drag

We explore the sensitivity of the gyre strength to the bottom drag curl by changing the bottom drag coefficient (halving the coefficient in DRAG0.5x and doubling it in DRAG2x). Not surprisingly, halving the bottom drag coefficient increases the Weddell Gyre strength and conversely, doubling the coefficient decreases its strength (Figure 2). The increase/decrease is small in magnitude (between 2 and 3 Sv difference with respect to roughly 50 Sv in CTRL), and is achieved during the first few years of the simulation. We integrate the terms in the BVB within the Weddell Gyre interior, which are are shown in Figure 5 as anomalies with respect to CTRL. Because most of these terms represent sinks of cyclonic vorticity for the Weddell Gyre (Figure 4b), positive values represent an increase in their role as sinks and negative values a decrease. The exception is surface stress curl, where negative values represent an increase in its role as a source of cyclonic vorticity.

The advection of planetary vorticity (Figure 5a) displays non-zero anomalies within the Weddell Gyre because there are slight displacements of the -17 Sv contour associated with expansions/contractions of the gyre that, unlike in the time-averaged BVB, yield a non-zero integration. There are also negligible variations in the surface stress curl (Figure 5b) because surface stress is computed using relative surface velocities and is thus dependent on the ocean's surface speed, but the overall role of this term as a source of cyclonic vorticity remains unchanged with respect to CTRL. The bottom drag curl anomalies (Figure 5c) show an increase in its role as sink of cyclonic vorticity for the increased bottom drag coefficient experiment, DRAG2x, with a symmetric and opposite decrease in the DRAG0.5x experiment. In other words, increasing the bottom drag coefficient increases the bottom drag curl's efficiency as a sink of cyclonic vorticity for the Weddell Gyre, with the opposite response in DRAG0.5x. The changes to bottom friction also alter the bottom boundary flows, which are felt near large topographic gradients by the horizontal viscous terms

(Figure 5d). With an increased bottom drag, the bottom flow weakens and so does the horizontal shear, reducing the role of $\hat{z} \cdot \nabla \times \mathcal{B}$ as a sink of cyclonic vorticity in DRAG2X and conversely for the DRAG0.5x experiment. Finally, although the nonlinear advection and BPT (Figure 5e and f respectively) display large variability, there is no clear net change in their role as source or sink with respect to CTRL.

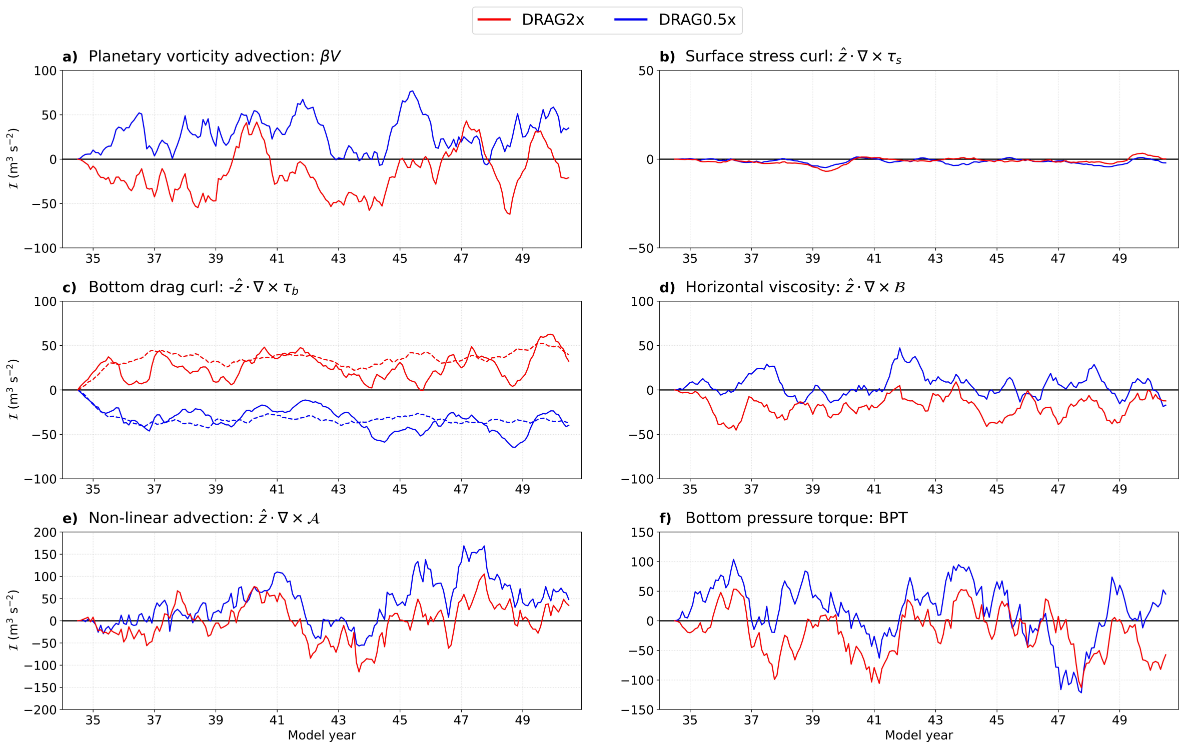

Fig. 5. Anomalies with respect to control of the BVB terms area integrated within the Weddell Gyre interior (blue region in Figure 4a) for the halved (DRAG0.5x) and doubled (DRAG2x) bottom drag coefficient simulations in blue and red respectively. For the bottom drag curl term in panel **c)** integration within the western boundary (hatched pink region in Figure 4a) is included in dashed lines. A 12-month running mean has been applied to all time series. Note that the vertical extent of each panel is different, but that the grid intervals are the same. Furthermore, positive values decrease the cyclonic (clockwise) Weddell Gyre strength relative to the CTRL experiment.

We also integrate the bottom drag curl within the western boundary region (dashed lines in Figure 5c), since we have identified this to be an area subject to important bottom friction in connection with DSW overflows (Figure 4b). Because the integration $\mathcal{I}$ depends on the size of the area A, and the area of the western boundary is much smaller than the area within the gyre interior, the changes in the bottom drag curl term at the western boundary are actually larger than in the interior. This result highlights the sensitivity of regions with DSW export to bottom friction.

The DRAG perturbation experiments are explicitly targeted at addressing the role of bottom friction in the Weddell Gyre's circulation. By looking at the changes relative to CTRL of the BVB terms integrated within different areas of the gyre, we are able to link changes in the bottom drag curl to changes in gyre strength, as well as identify the region where those changes are dominant: namely the western boundary current system. In this region, DSW export is associated with a significant bottom-intensified flow, making the circulation particularly sensitive to bottom friction. We next consider a subsequent suite of perturbations aimed at achieving changes in bottom drag at the western boundary by changing the bottom flow through perturbations to DSW production and export.

c. Role of Dense Shelf Water overflows

For the MW perturbation experiments, we increase (MW+) and decrease (MW-) meltwater input at the surface around the Antarctic margin by 50%. Changes in meltwater input impact surface water mass transformations at the continental shelf, and subsequently the formation rates and characteristics of DSW. Figure 6a shows surface water mass transformation in the Weddell's south western continental shelf in the vicinity of the Filchner-Ronne Ice Shelf for the CTRL simulation and MW experiments. Increasing MW input shifts the density of the waters produced on the shelf to lighter varieties and in turn, the export of DSW across the 1000m isobath to the open abyssal ocean is reduced in volume and density (Figure 6b and c respectively). Conversely, removing meltwater input shifts surface water mass transformation towards denser classes of DSW and increases the volume and density of export across the continental slope.

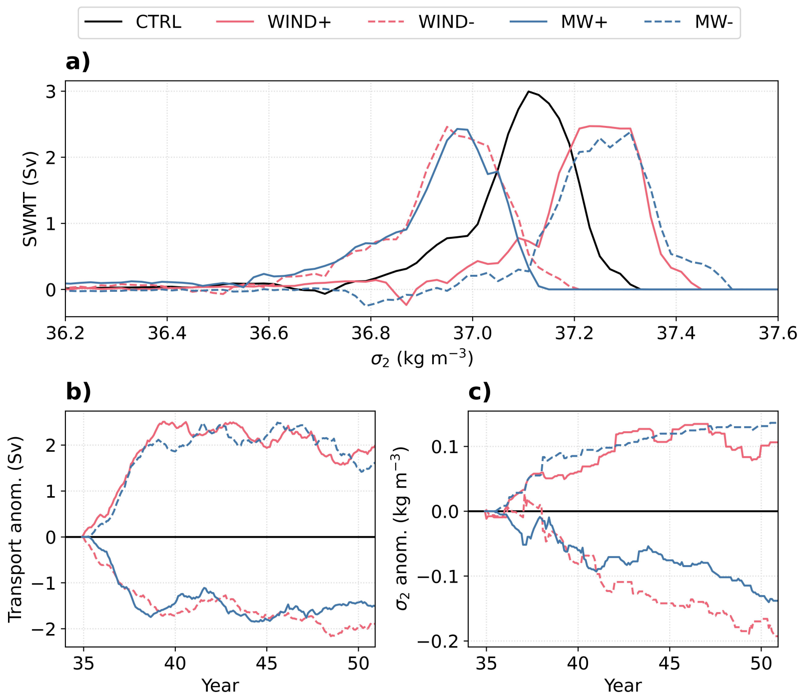

FIG. 6. **a)** Surface water mass transformation at the Weddell's southwestern continental shelf calculated from heat and salt fluxes (Newsom et al. 2016) for the control simulation (CTRL), increased (MW+) and decreased (MW-) meltwater experiments as well as the increased (WIND+) and reduced (WIND-) surface wind velocities experiments. **b)** DSW export across the 1000m isobath as anomalies with respect to CTRL, calculated following Morrison et al. (2023) as the off-shore volume transport across the 1000m isobath, first integrated along the isobath and then cumulatively summed across density layers from the densest layer up to the density layer where the cumulative transport is maximum. The density threshold used for **b)** are shown in **c)** as anomalies with respect to CTRL.

Gyre strength displays monotonic trends in the MW experiments, with a trend towards a stronger gyre in MW+ and a weaker gyre in MW- (Figure 2). Unlike the DRAG experiments, the response is not symmetric between MW+ and MW-, with the latter inducing a stronger trend in gyre strength. The anomalies with respect to CTRL of the integrated terms of the BVB budget are shown in Figure 7. In the MW- experiment, the weakening of the gyre drives a contraction of the -17 Sv contour (not shown) that impacts the planetary vorticity advection and surface stress curl terms (Figure 7a and b respectively). The contraction of the area is associated with reduced ocean surface velocities, which implies an increase in the relative surface stress and therefore an increase in the role of surface stress as source of cyclonic vorticity (blue line in Figure 7b). In the MW+ experiment, there is little change in the position of the -17 Sv contour, and therefore the changes to surface stress curl are negligible compared to MW-.

As expected from the changes in DSW export, the MW- experiments show marked changes in the bottom drag curl term (Figure 7c). For the MW- experiment, there is an increase in the role of the bottom drag curl as sink of cyclonic vorticity that is linked to the increased export of DSW and enhanced bottom friction. The changes in the bottom drag curl term integrated at the western boundary region are of similar magnitude as the integration in the gyre interior. As detailed for the DRAG experiments, similar magnitudes in the integration indicate larger changes in bottom drag at the western boundary than the interior.

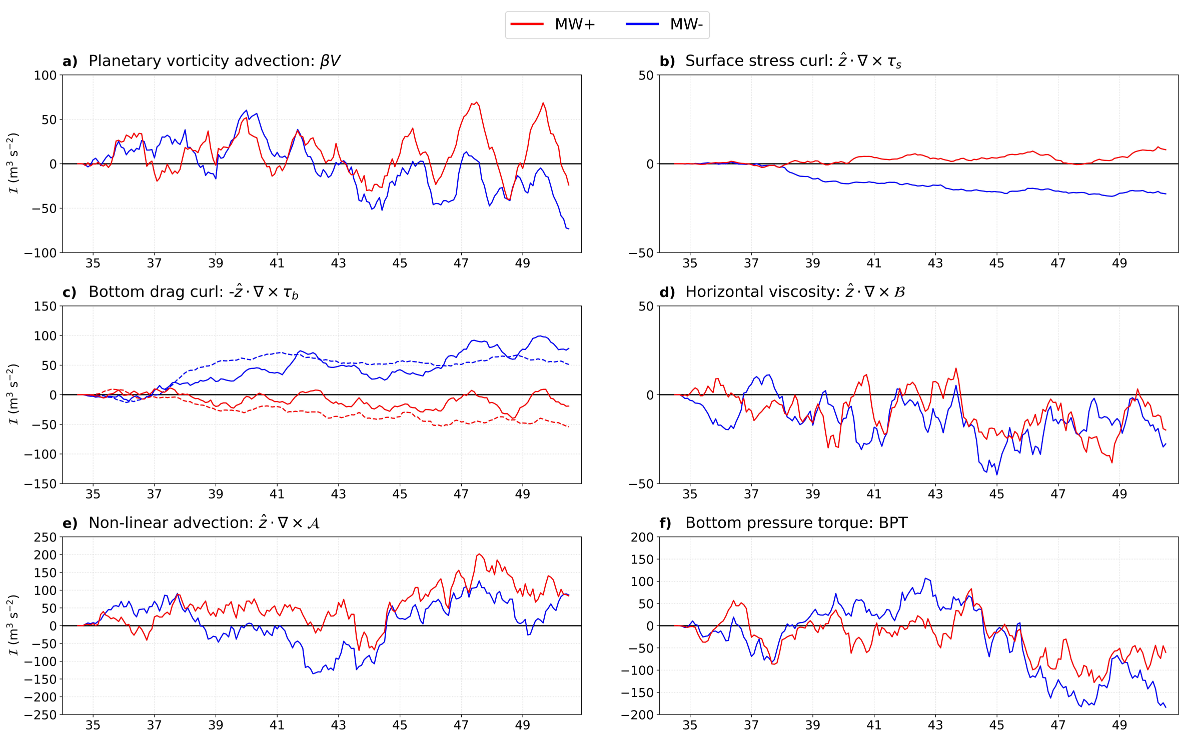

FIG. 7. Anomalies with respect to control of the BVB terms integrated within the Weddell Gyre interior (blue region in Figure 4a) for the reduced (MW-) and increased (MW+) meltwater simulations in blue and red respectively. For the bottom drag curl term in panel **c)** the integration within the western boundary (hatched pink region in Figure 4a) is included in dashed lines. A 12-month running mean has been applied to all time series. Note that the extent of each panel is different, but that the grid intervals have been kept the same.

Figure 8 shows cross sections of potential density and transport at two different locations. In Figures 8b and d, the cross section is located within a region with DSW overflows within the western boundary. The strengthened overflow is visible in the increase in densities along the continental slope (Figure 8b) and in the increased northward transport at the bottom (Figure 8d). Above the stronger bottom layer, there is a weakening of the northward transport, associated with the decrease in bottom friction and a decrease in the isopycnal tilt towards the coast, where isopycnals that previously outcropped onto the continental slope now display a connection with the shelf. The other cross sections in Figure 8c and e are located at the Greenwich Meridian, in a region of the gyre's boundary current system that is not subject to DSW overflows. The removal of meltwater at the boundaries lifts the isopycnals and reduces their tilt, weakening the westward transport throughout the water column. Overall, these cross sections show that the changes in the circulation are concentrated at the boundaries rather than in the gyre interior.

The MW+ experiment shows the opposite response in the bottom drag curl term compared to MW-, with a decrease in the role of bottom drag curl as a sink of cyclonic vorticity that is again larger for the western boundary (Figure 7c). This response is dampened in MW+ compared to MW- because in this case, a decrease in DSW export and a shift towards lighter densities means that the response is confined to shallower layers and is not penetrating as deep as in MW-. The asymmetry in the response to DSW overflow is behind the asymmetry in gyre strength changes (Figure 2).

For the MW+ simulation, cross-sections within the western boundary show the reduced connection between the continental shelf and the open ocean. The reduction in DSW export is visible in a thin layer of weaker northward transport at the bottom (Figure 9d) and an increase in isopycnal tilt (Figure 9b). Isopycnals that in CTRL connect the shelf and the deeper ocean, in MW+ intersect with the slope. The increase in isopycnal tilt, together with reduced bottom friction, drive an overall increase in the northward transport throughout the water column (Figure 9d). Outside of DSW export regions, increasing meltwater input pushes the isopycnals downwards toward the coast, increasing the horizontal density gradient, thus increasing the westward transport at the southern boundary in the ASC (Figure 9c and e). As in the MW- experiment, these cross sections show that the largest response is confined to the boundaries of the Weddell Gyre.

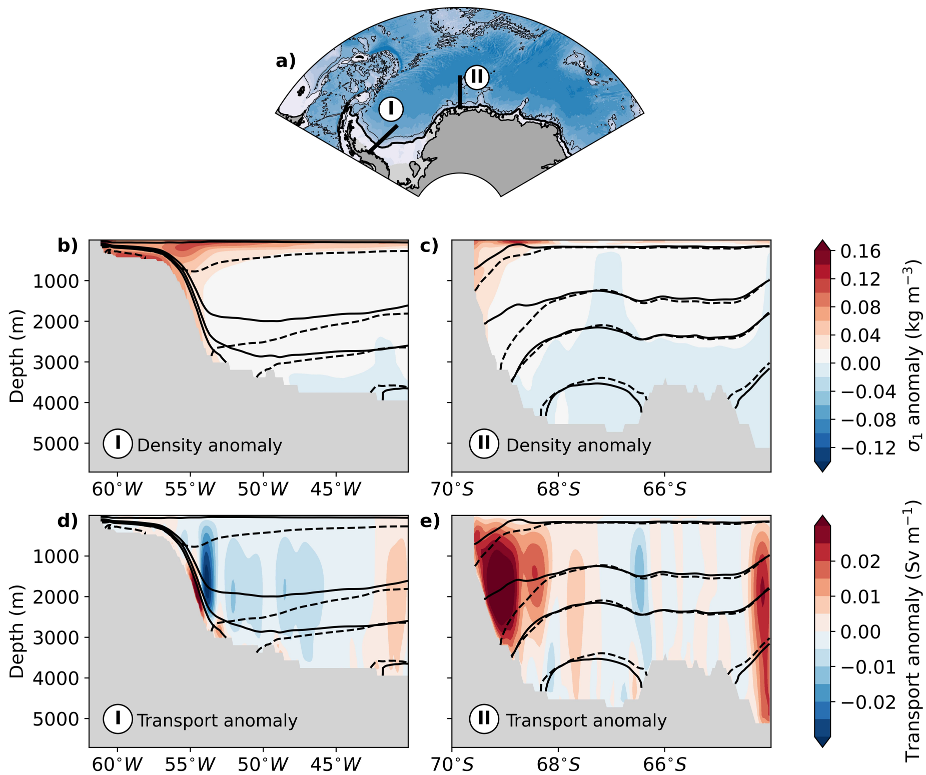

FIG. 8. Panel **a)** depicts the two transects considered in the following panels, with transect I at 70°S, and transect II at 0°E. Panel **b)** shows anomalous potential density (referenced to 1000 dbar) and **d)** meridional transport for the MW- experiment along the transect I averaged over the final five years of the experiment. Panels **c)** and **e)** show the same as panels **b)** and **d)**, yet for transect II. Contours in panels **b)** to **e)** show four different isopycnals for control (black dashed) and MW- simulations (black solid)

To summarize, our MW simulations induce a response in DSW production and export that is able to drive changes in gyre strength via bottom friction. In the MW- simulation, the increase in DSW export strengthens the bottom circulation in overflowing locations, particularly at the western boundary region. A stronger bottom flow is associated with increased bottom drag, which drives an overall weakening of the gyre's boundary transport above the bottom layer. While the response associated with bottom friction is confined to the western boundary, outside of DSW formation regions the reduction in meltwater reduces the horizontal density gradients, lifting isopycnals towards the coast and overall weakening the westward transport throughout the water column. Conversely, in the MW+ experiment the decreased DSW export is associated with a weaker bottom flow in DSW overflowing regions and an increase in the horizontal density gradients outside of

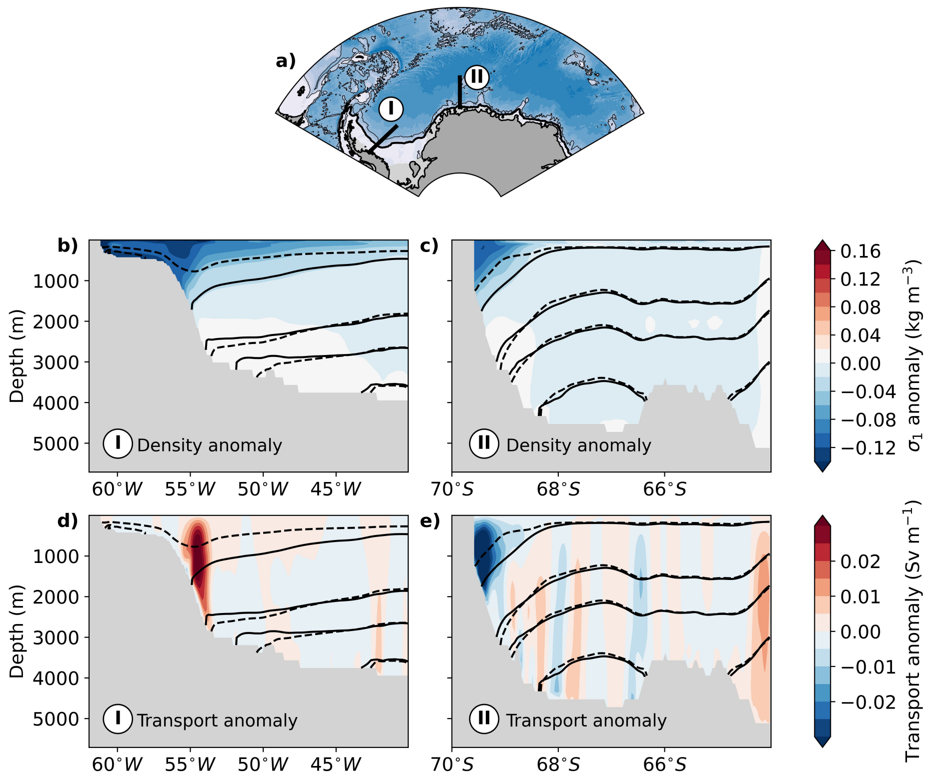

FIG. 9. Panel **a)** depicts the two transects considered in the following panels, with transect I at 70°S, and transect II at 0°E. Panel **b)** shows anomalous potential density (referenced to 1000 dbar) and **d)** meridional transport for the MW+ experiment along the transect I averaged over the final five years of the experiment. Panels **c)** and **e)** show the same as panels **b)** and **d)**, yet for transect II. Contours in panels **b)** to **e)** show four different isopycnals for control (black dashed) and MW+ simulations (black solid)

DSW overflowing regions. The end result is a stronger boundary current less subject to bottom friction effects, and stronger transport via the thermal wind relation. The response in gyre strength is not symmetric between MW- and MW+, because MW+ involves a reduced and lighter export of DSW, confining the response to shallower layers than the increased, denser export in MW- that is able to penetrate deeper into the gyre.

d. Role of surface stress

The DRAG and MW experiments have explored the role of bottom friction as a sink of cyclonic vorticity, and its influence on the Weddell Gyre strength, without changing the mechanisms that act as a source of cyclonic vorticity. Our final suite of experiments address the role of surface stress curl, which is traditionally assumed to force ocean gyres and is the only source of cyclonic vorticity for the Weddell Gyre (Figure 4b). We increase (WIND+) and decrease (WIND-) surface winds by 10%, noting that this change will also have an effect on the contribution of sea ice to surface stress.

There are two time scales in the response of gyre strength to changes in surface winds (Figure 2). During the first year of the perturbation there is a direct response wherein increasing the winds in WIND+ strengthens the gyre and vice versa for WIND-, with Ekman effects at the surface dominating the response in gyre transport. After the first year, there is an inversion in the response, with WIND+ counterintuitively showing a steady weakening of the gyre and WIND- a steady strengthening. The longer term trends in the WIND experiments closely resemble those of the MW experiments, even in their asymmetry with respect to CTRL, with WIND+ showing a larger weakening towards the end of the simulations than the strengthening found in WIND-.

Figure 10 shows the integrated terms of the BVB for the WIND simulations. In the WIND experiments changing the surface wind field involves a more complex response from the coupled ocean/sea ice system, instead of a response focused on a single term of the BVB in the DRAG experiments, namely bottom friction. The increased complexity of these perturbations compared to the DRAG and MW experiments is reflected in the more intricate response of the BVB terms. Surface stress curl (Figure 10a) shows a clear increase in its role as a source of cyclonic vorticity in WIND+ with a mirror-image like decrease obtained in WIND-. Most of the changes to surface stress curl are compensated by an opposite change in the BPT (Figure 10f) that is achieved during the first year of the simulation. The implication is that interactions with topography via the BPT balance surface stress, as was observed for the time-mean balance of the CTRL simulation (Figure 4b).

However, changes in surface winds also change surface water mass transformations and DSW formation on the shelf via changes to sea ice advection (Morrison et al. 2023) and subsequent export of DSW across the 1000m isobath. In the case of our WIND simulations, the changes are similar in magnitude and timing to those found in the MW experiments (Figure 6). Via increased sea-ice formation and export, WIND+ shifts surface water mass transformation towards denser classes and increases the export rate and density of DSW, with the opposite sign response for WIND-. We can link these changes in DSW export to changes in gyre strength via the same

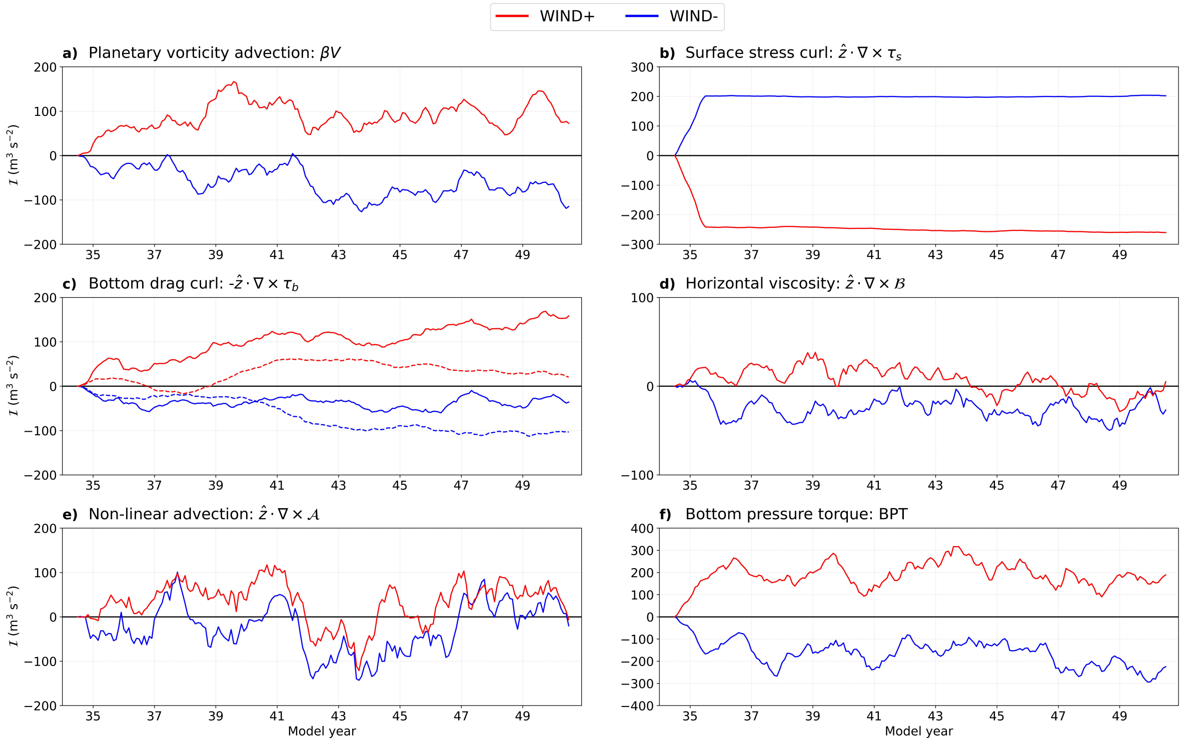

FIG. 10. Anomalies with respect to control of the BVB terms integrated within the Weddell Gyre interior (blue region in Figure 4a) for the reduced (WIND-) and increased (WIND+) surface winds simulations in blue and red respectively. For the bottom drag curl term in panel **c)** the integration within the western boundary (hatched pink region in Figure 4a) is included in dashed lines. A 12-month running mean has been applied to all time series. Note that the extent of each panel is different, but that the grid intervals have been kept the same.

mechanism proposed in the MW experiments. Namely, for WIND+, an increase in DSW export increases the role of the bottom drag curl as a sink of cyclonic vorticity (Figure 10c) and therefore weakens the gyre strength on timescales longer than a couple of years. For the WIND- simulation, the reduced overflow confined to shallower layers induces a more modest response in bottom drag that is linked to the strengthening observed in gyre strength towards the end of the simulations. As in the previous experiments, the response of the western boundary region to changes in DSW export and bottom drag is larger than in the interior.

The changes to the vertical structure in the WIND experiments (not shown) mimic those of the MW experiments. As in MW-, WIND+ shows an increased bottom flow associated with the denser overflows at the western boundary, and a decrease in the isopycnal tilt that weakens the thermal wind transport. On the other hand, as in MW+, WIND- shows the weakened bottom flow associated with the reduced export, an increase in horizontal density gradients and an overall stronger transport. As was explored in the MW experiments, the response in bottom drag curl is not symmetric between WIND+ and WIND- experiments because lighter export is not penetrating as deep into the gyre as a denser export.

e. Gyre strength changes during model spin-up

Using a barotropic vorticity budget and sensitivity experiments, we have identified the processes involved in driving variability in gyre strength, as well as the regions in which these processes dominate. Using the knowledge acquired with the perturbation experiments, we can now also explain the ∼15 Sv increase in gyre strength that occurs during model spin-up (Figure 2). This change does not come from changes in the forcing (i.e. surface stress), since our model is forced

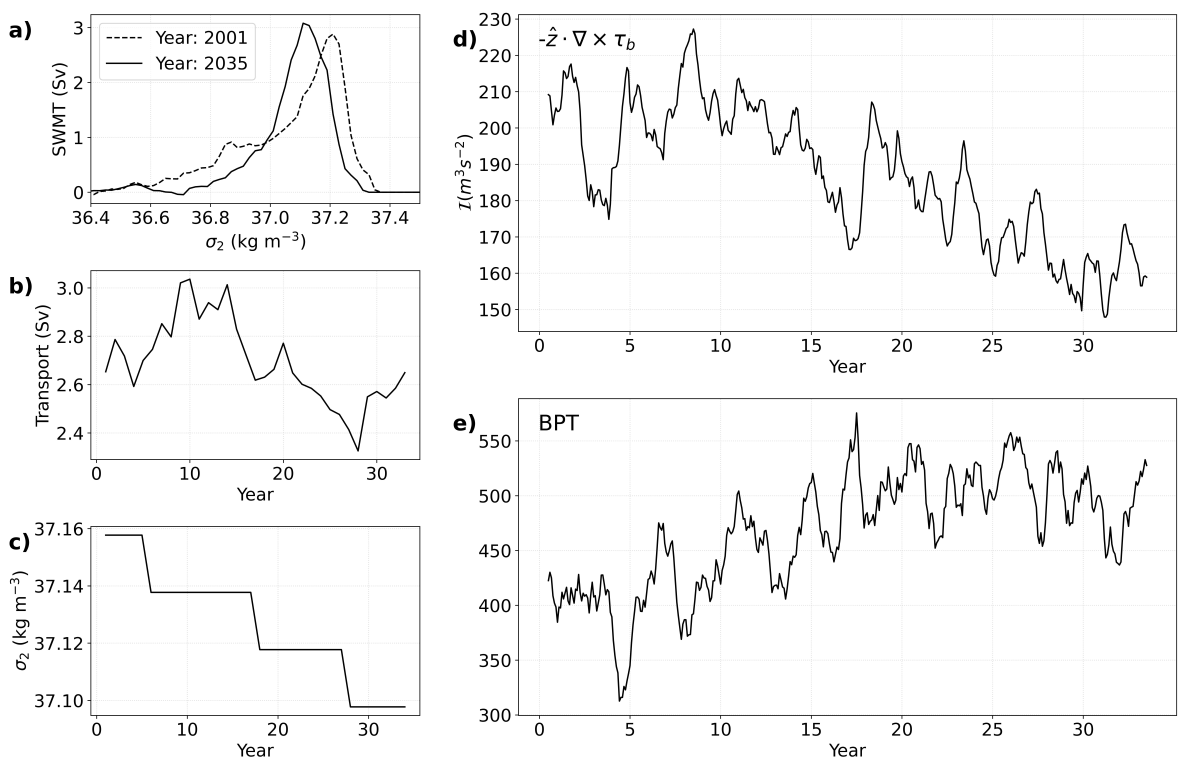

FIG. 11. **a)** Surface water mass transformation at the southwestern continental shelf for the control simulation the first year of spin-up (dashed line) and last year of spin-up (solid line). **b)** Export and **c)** density of export of DSW across the 1000m isobath and **d)** time series of the bottom drag curl ($-\hat{z}\cdot\nabla\times\tau_{\mathbf{b}}$) and **e)** bottom pressure torque (BPT) during the spin-up period.

with the same atmospheric year on repeat, and is instead related to model adjustment.

In particular, during model spin-up, there are changes to DSW formation. The continental shelf becomes fresher and therefore surface water mass transformation shifts toward a lighter DSW production and a reduction in its export across the 1000m isobath (Figure 11a, b and c). The drift in the overflow drives a decrease in the role of bottom drag curl, particularly at the western boundary. As a result, the gyre spins-up, and with a stronger flow the BPT adjusts to balance the input of cyclonic vorticity by the surface stress curl (Figure 11d). The changes in density structure at the southern boundary are similar to those described in the MW+ and WIND- experiments.

5. Summary and Discussion

In this work we have used for the first time a barotropic vorticity budget to study the adjustment of the Weddell Gyre circulation to perturbations in forcing mechanisms. Unlike past studies that have focused on an equilibrium state to identify sources and sinks of vorticity (Le Corre et al. 2020; Schoonover et al. 2016; Sonnewald et al. 2023, 2019; Yeager 2015), our study investigates how the gyre adjusts to forced changes by analysing the transient response of the terms in the barotropic vorticity budget, identifying the key physical mechanisms that can induce variations in gyre strength. We carry out three different perturbation experiments in which we separately change the bottom drag coefficient, meltwater input at the Antarctic coastline and surface winds.

We characterise the mean state of our control simulation and find that the main balance in equilibrium is established between the surface stress curl as a source of cyclonic vorticity and the bottom pressure torque as a sink (Figure 4), in line with past studies carried out in the North Atlantic subtropical gyre (e.g., Hughes 2000; Hughes and De Cuevas 2001; Yeager 2015; Schoonover et al. 2016). Additionally, we find that the bottom drag curl, horizontal viscosity and nonlinear terms each contribute as a sink in cyclonic vorticity, with particular significance of bottom friction at the western boundary. The dominance of bottom friction at the western boundary is not surprising considering the bottom-intensified flow that characterises the region in connection with Dense Shelf Water production upstream at the Filchner-Ronne Ice Shelf.

To assess the role of bottom drag, our first suite of experiments increased or decreased the bottom drag coefficient. The gyre's horizontal circulation adjusts rapidly to changes in bottom drag, increasing gyre strength with a reduced drag coefficient and vice versa for increased drag coefficient (Figure 2). Namely, a higher drag coefficient makes the bottom flow a more efficient sink of cyclonic vorticity (Figure 5c). The western boundary region of the gyre experiences changes in bottom drag curl larger than those seen in the interior of the gyre. This result highlights the importance of friction in areas where Dense Shelf Water overflows provide a significant bottom component to the circulation. The DRAG experiments show the sensitivity of gyre strength to bottom friction and pinpoint the regions where most of the adjustments occur in connection with bottom intensified flows associated with Dense Shelf Water export.

To further explore the role of Dense Shelf Water overflows we next considered meltwater anomaly experiments, locally adding or removing meltwater at the Antarctic margins. The change in salinity at the surface drives changes in surface water mass transformation that translate into changes in Dense Shelf Water production and export across the 1000m isobath into the gyre (Figure 6). Therefore, the meltwater experiments alter the strength of the bottom flow at the western boundary. Increasing meltwater input decreases the export volume and density of Dense Shelf Water, which weakens the bottom flow at the continental slope (Figure 9). As a consequence of the weakened bottom circulation, the western boundary downstream of the Filchner-Ronne Ice Shelf experiences reduced bottom friction (Figure 10c), driving an increase in gyre strength (Figure 2). Decreasing meltwater input has the opposite response in gyre strength and bottom drag curl, albeit larger in magnitude because denser overflows are able to penetrate deeper into the water column after overflowing the continental shelf, whereas the lighter overflow in the increased meltwater experiment is confined to shallower layers.

Our final suite of experiments addressed the response in gyre strength to changes in surface stress by increasing or decreasing the wind speed over the entire model domain. This perturbation is relevant because, traditionally, surface stress is assumed to be the driving force of ocean gyres, and most studies propose a direct relationship between surface stress and gyre strength, wherein a stronger surface cyclonic stress curl implies a stronger gyre (Meredith et al. 2011; Gordon et al. 2020). We observe this direct response during the first year or so of our simulations, with the initial increase in surface stress balanced almost entirely by the bottom pressure torque term. However, on timescales longer than a couple of years the response in gyre strength reverses, displaying a monotonic trend towards a weaker gyre (Figure 2), which highlights the complexity of the response of the barotropic transport to changing winds in this region.

We attribute the longer term response in gyre strength in the wind experiments to changes in Dense Shelf Water formation and export. Increasing surface winds drive, in the long term, an increase in Dense Shelf Water production and export (Figure 6). Consistent with the meltwater experiments, there are associated changes to the overflow of dense waters at the western boundary and therefore changes to bottom friction. The stronger overflows sustained by increased winds enhance the efficiency of bottom friction as a sink of cyclonic vorticity, with the opposite response seen when the winds are decreased (Figure 10c). These processes are illustrated in Figure 12. The response of Dense Shelf Water production to surface winds is consistent with past modeling and observational studies. For example, Morrison et al. (2023) examine the sensitivity of Dense Shelf Water production to changes in surface winds around the Antarctic margins, and find that decreased winds reduce sea ice export northwards, which decreases sea ice production and therefore the salinity on the shelf. The net effect is a reduction in Dense Shelf Water production after a couple of years. The link between surface winds/sea ice/Dense Shelf Water production has also been reported to be behind the volume contraction of bottom waters recently observed within the Weddell Gyre due to decreased sea ice production and weakening winds (Zhou et al. 2023).

One of the interesting aspects of this work is that bottom friction, acting as a sink of cyclonic vorticity, is able to mediate changes to gyre strength. We were able to arrive at this finding because we worked with a time-varying framework alongside perturbation simulations. Most past studies using a barotropic vorticity budget focus on a time-averaged control simulation, such as our Figure 4, where bottom friction appears to have a secondary contribution. Without the perturbation simulations and the analysis of the transient response, the dominant role of Dense Shelf Water overflows would unlikely have come to light. This result also has implications for numerical model representation of the Weddell Gyre: namely accurately representing bottom flows around the gyre's boundaries are key to accurately representing the gyre's mean transport and variability.

One of the original motivations of this study was to better understand the year-to-year and decadal variability of the Weddell Gyre's transport. A past model study that characterised the variability in strength found significant interannual variability with extreme events of circulation that induced significant changes to the gyre's horizontal transport and hydrography of the region (Neme et al.

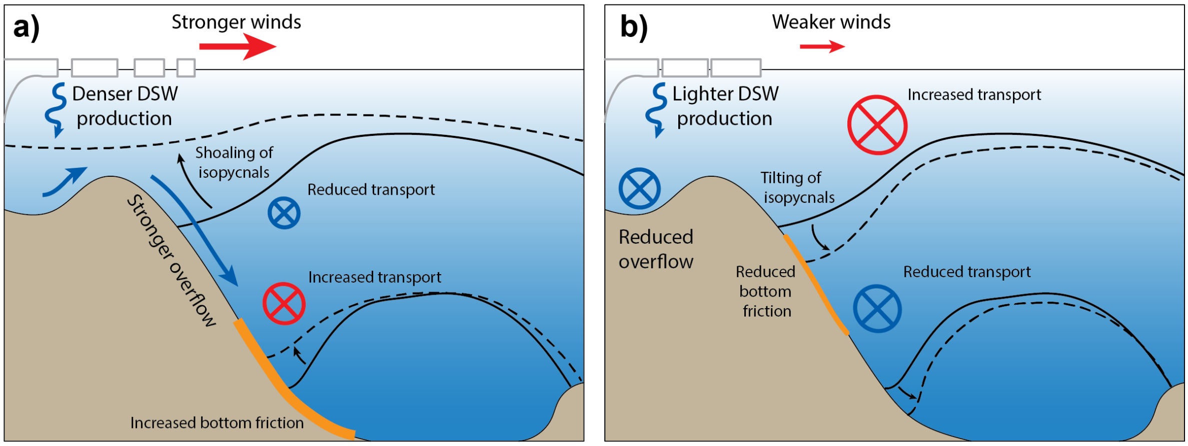

FIG. 12. Schematics showing the controlling dynamics and response to **a)** increasing surface winds and **b)** decreasing surface winds. Perturbations to the wind field drive changes to Dense Shelf Water (DSW) formation and export, which alter the bottom flow at the boundary and therefore the removal of cyclonic vorticity via bottom friction at the continental slope. Increasing bottom friction in **a)** drives a barotropic weakening of the Weddell Gyre boundary, which is accompanied by a decrease in the horizontal density gradients. The opposite response occurs in **b)**, albeit confined to shallower layers due to the decreased density of the overflow. In this schematic, we only depict the cross-shore component of surface winds which is the one related to DSW production changes according to the works of Morrison et al. (2023) and Zhou et al. (2023).

2021). Yet, Neme et al. (2021) only found a weak correlation (0.51 with $p < 0.05$) between gyre strength and local easterly winds, and no significant links were found for either surface stress curl or surface buoyancy fluxes. The results of the present study can help explain why Neme et al. (2021) could not identify a clear dominant driver, as we have shown that there are two distinct time scales and processes involved in the gyre's response to wind forcing. Namely, there is a rapid time scale response to surface winds during the first year that involves a direct response in gyre strength, following a topographic-Sverdrup like balance à la Hughes (2000). However, the longer-term response is dominated by changes to buoyancy forcing close to the Antarctic margins. These buoyancy changes can themselves be wind-forced, as suggested by observational and modelling studies (McKee et al. 2011; Morrison et al. 2023; Zhou et al. 2023). Our model configuration, examining perturbations to a repeat year control simulation, allows us to isolate these responses. However, in the real system and in the interannually forced model of Neme et al. (2021), the rich array of forcing variability would drive an even richer array of responses in the Weddell Gyre's strength. Disentangling the response and attributing the changes in gyre strength to driving factors would thus prove difficult.

We employ a high-resolution ocean/sea ice model that is able to accurately reproduce the formation process of bottom waters at selected locations around the continental margins and its export across the 1000m isobath. Hence, even though the model lacks ice shelf cavities, we consider that its representation of the bottom circulation adjacent to Dense Shelf Water export locations is adequate for the purposes of this work. Our meltwater sensitivity experiments are targeted to modifying the export of bottom waters from the shelf to the abyssal ocean, and therefore the bottom flow along the gyre's boundaries. Our wind experiments also achieve, on timescales longer than a couple of years, changes to bottom water formation and export. These changes are consistent with those suggested by observational studies, wherein stronger winds intensify bottom water production through enhanced sea ice advection (McKee et al. 2011; Zhou et al. 2023). However, the magnitude and timing of the response we observe in our experiments is possibly sensitive to the addition of ice shelf cavities and the introduction of basal melt at depth. This qualification does not influence our results regarding the role of bottom friction in relation to the Weddell Gyre strength. A final caveat is that around the Antarctic margins our model is not eddy-resolving and so does not fully resolve the mesoscale field. The role of eddies in cross-shelf transport is well known (Stewart and Thompson 2015, 2016), and it is possible that in a higher resolution model that fully resolves the eddy field, the role of the nonlinear advection term in Equation (1) gains relative importance. This question will remain the subject of future research.

6. Conclusions

We have used for the first time a barotropic vorticity budget to investigate the mechanisms behind transient responses in Weddell Gyre strength to forced changes. While in an equilibrium state the dominant balance is established between the surface stress curl and bottom pressure torque, we carry out perturbation experiments that highlight the influence of different processes in setting gyre strength, namely bottom friction, including that induced by meltwater anomalies and wind variations. Due to the vicinity of the Weddell Gyre to a Dense Shelf Water production region at the Filchner-Ronne Ice shelf, the western boundary current system of the gyre experiences a strong bottom circulation associated with the cascading of dense waters across the continental slope into the gyre interior. Such strong bottom flow allows for a frictional sink of cyclonic vorticity in this region that when perturbed can drive changes to gyre strength.

In particular, we found that modification of the dense overflows and bottom friction at the western boundary can be achieved via changes to meltwater input or changes to surface winds. As shown in model studies and observations (Morrison et al. 2023; Zhou et al. 2023), one of the longer term responses of the ocean to changes in surface winds is changes to formation and export of bottom waters, wherein decreased bottom water formation is associated with weaker winds. Our results are consistent with this mechanism and show that, if weakened winds drive a decrease in bottom water production, the Weddell Gyre will strengthen in response to weaker bottom friction. This result challenges the traditional assumption of a direct relationship between gyre strength and surface stress curl, which only holds true for the initial year of our perturbation experiments.

Our model simulations are intended to isolate perturbations to the system and therefore we chose an experimental design that included no interannual variability. In the real world, on interannual timescales, the intrinsic variations of surface stress and buoyancy forcings, together with the different timescales in the Weddell Gyre's response, will likely make it difficult to isolate individual driving processes. We propose this is a contributing factor to the current uncertainty in the drivers of variability of Weddell Gyre strength on interannual time-scales. Our results can also contribute to an improved understanding of future changes in the Weddell Gyre circulation. For example, in the absence of other changes, our study suggests that a slowdown of Dense Shelf Water production (Li et al. 2023; Lago and England 2019) associated with increased Antarctic ice melt (Golledge et al. 2015) alongside weakened Antarctic margins winds (Neme et al. 2022), in combination with poleward shifting westerlies (Goyal et al. 2021) would each individually and in combination contribute to a strengthening of the Weddell Gyre. With suitable measurement platforms in place, these changes should mature and become detectable over the coming decades.

Acknowledgments. This work was supported by the Australian Research Council, including the ARC Centre of Excellence for Climate Extremes and the ARC Centre of Excellence for Antarctic Science. Numerical simulations and analysis were conducted at the NCI National Facility systems at the Australian National University through the National Computational Merit Allocation Scheme. HK acknowledges the support from UK NERC grant NE/T013494/1. The authors thank the COSIMA consortium, and in particular Angus Gibson, for its support and constructive discussions, as well as the two anonymous reviewers and Jan-Erik Tesdal for their time reviewing this manuscript and contributing to its clarity.

Data availability statement. The source code for our model simulations can be found at `https://github.com/COSIMA/mom6-panan`. The analysis code used to produce the figures will be available at `GITHUB`.

APPENDIX A

Derivation of the Barotropic Vorticity Budget

Here we derive the barotropic vorticity budget in Equation (1). We start from the continuous velocity equation using the Boussinesq approximation, as given in Adcroft et al. (2019)

$$\partial_t \mathbf{u} + (f+\zeta)\hat{\mathbf{z}} \times \mathbf{u} + w^{(\dot{r})}\partial_r \mathbf{u} = -[\rho_0^{-1}\nabla_r p + \nabla_r \Phi] - \nabla_r K + \mathcal{F} + \rho_0^{-1}\partial_r \tau \tag{A1}$$

where $r = r(x,y,z,t)$ is a generalized vertical coordinate and $\mathbf{u} = \hat{\mathbf{x}}u + \hat{\mathbf{y}}v$ is the horizontal velocity vector. $w^{(\dot{r})} = \partial_r z D_t r$ is a dia-surface velocity used for remapping, $\nabla_r = \hat{\mathbf{x}}[\frac{\partial}{\partial x}]_r + \hat{\mathbf{y}}[\frac{\partial}{\partial y}]_r$ is the horizontal gradient on the r surfaces, $-[\rho_0^{-1}\nabla_r p + \nabla_r \Phi]$ is the horizontal pressure acceleration with $\Phi = gz$. $K = (u^2+v^2)/2$ is the horizontal kinetic energy per mass, and $\mathcal{F} = \mathcal{F}^{vert} + \mathcal{F}^{horz}$ includes horizontal and vertical diffusion. Finally $\partial_r \tau = \delta(z-\eta)\tau_\mathbf{s} - \delta(z-H)\tau_\mathbf{b}$ combines surface stress ($\tau_\mathbf{s}$) and bottom drag ($\tau_\mathbf{b}$), with Dirac's delta (δ).

We first integrate Equation (A1) from the ocean's bottom, $z = -H(x,y)$, to the surface, $z = \eta(z,y,t)$, to obtain

$$\int_{-H}^{\eta} \partial_t \mathbf{u} dz = -f\hat{\mathbf{z}} \times \int_{-H}^{\eta} \mathbf{u} dz - \frac{1}{\rho_0}\int_{-H}^{\eta} \nabla p dz + \frac{\tau_\mathbf{s}}{\rho_0} - \frac{\tau_\mathbf{b}}{\rho_0} + \int_{-H}^{\eta} \mathbf{a} dz + \int_{-H}^{\eta} \mathbf{b} dz, \tag{A2}$$

where $\mathbf{a} = -\zeta\hat{\mathbf{z}}\times\mathbf{u} - \nabla_r K - w^{(\dot{r})}\partial_r\mathbf{u}$ and $b = \mathcal{F}^{horz}$ because the vertical integral of $\mathcal{F}^{vert}$ over the whole depth vanishes. Note that we have replaced $\nabla_r p$ by ∇p, where $\nabla = \hat{\mathbf{x}}\partial_\mathbf{x} + \hat{\mathbf{y}}\partial_\mathbf{y}$ because when working with the vertically-integrated velocity equation the following steps are independent of the choice of vertical coordinate.

For simplicity, we introduce $\mathcal{U}_t = \int_{-H}^{\eta}\partial_t\mathbf{u}dz$, $\mathcal{A} = \int_{-H}^{\eta}\mathbf{a}dz$ and $\mathcal{B} = \int_{-H}^{\eta}\mathbf{b}dz$ and apply the Leibniz integral rule to the pressure gradient term to obtain:

$$\mathcal{U}_t = -f\hat{\mathbf{z}}\times\int_{-H}^{\eta}\mathbf{u}dz - \frac{1}{\rho_0}\nabla\left[\int_{-H}^{\eta}pdz\right] + p_s\nabla\eta + p_b\nabla H + \frac{\tau_\mathbf{s}}{\rho_0} - \frac{\tau_\mathbf{b}}{\rho_0} + \mathcal{A} + \mathcal{B}. \tag{A3}$$

The terms $p_s\nabla\eta$ and $p_b\nabla H$ are form stresses at the ocean's surface and bottom respectively, with p_s and p_b pressures at the surface and bottom of the ocean. We take the curl of Equation (A3)

$$\begin{aligned}\hat{\mathbf{z}}\cdot\nabla\times\mathcal{U}_t = &-\hat{\mathbf{z}}\cdot\nabla\times\left(f\hat{\mathbf{z}}\times\int_{-H}^{\eta}\mathbf{u}dz\right) - \frac{1}{\rho_0}\nabla\times\left(\nabla\left[\int_{-H}^{\eta}pdz\right] - p_s\nabla\eta - p_b\nabla H\right)\\ &+\hat{\mathbf{z}}\cdot\frac{\nabla\times\tau_\mathbf{s}}{\rho_0} - \hat{\mathbf{z}}\cdot\frac{\nabla\times\tau_\mathbf{b}}{\rho_0} + \hat{\mathbf{z}}\cdot\nabla\times\mathcal{A} + \hat{\mathbf{z}}\cdot\nabla\times\mathcal{B}\end{aligned} \tag{A4}$$

The Coriolis term (first term in right hand side of Equation A4 can be split into two: $\hat{\mathbf{z}}\cdot\nabla\times\left(f\hat{\mathbf{z}}\times\int_{-H}^{\eta}\mathbf{u}dz\right) = \beta\int_{-H}^{\eta}vdz + f\nabla\cdot\int_{-H}^{\eta}\mathbf{u}dz$. By the conservation of volume for a vertical column of a Boussinesq fluid, we can further split $\nabla\cdot\int_{-H}^{\eta}\mathbf{u}dz = Q_m/\rho_0 - \partial_t\eta$. Furthermore, the second term on the right hand side of Equation A4, can be written as $1/\rho_0(J(p_s,\eta) + J(p_b,H))$, where J is the Jacobian operator. The model imposes a uniform pressure at the ocean surface, so that $J(p_s,\eta) = 0$.

With the above considerations and writing the depth-integrated meridional transport as $V = \int_{-H}^{\eta}vdz$, Equation A4 can be written as

$$\beta V = \frac{J(p_b,H)}{\rho_0} - \frac{fQ_m}{\rho_0} + f\partial_t\eta - \hat{z}\cdot\nabla\times\mathcal{U}_t + \frac{\hat{z}\cdot\nabla\times\tau_\mathbf{s}}{\rho_0} - \frac{\hat{z}\cdot\nabla\times\tau_\mathbf{b}}{\rho_0} + \hat{z}\cdot\nabla\times\mathcal{A} + \hat{z}\cdot\nabla\times\mathcal{B}. \tag{A5}$$

References

Abrahamsen, E. P., and Coauthors, 2019: Stabilization of dense Antarctic water supply to the Atlantic Ocean overturning circulation. *Nature Climate Change*, **9 (10)**, 742–746.

Adcroft, A., and J.-M. Campin, 2004: Rescaled height coordinates for accurate representation of free-surface flows in ocean circulation models. *Ocean Modelling*, **7 (3-4)**, 269–284.

Adcroft, A., and Coauthors, 2019: The GFDL global ocean and sea ice model OM4. 0: Model description and simulation features. *Journal of Advances in Modeling Earth Systems*, **11 (10)**, 3167–3211.

Auger, M., J.-B. Sallée, P. Prandi, and A. C. Naveira Garabato, 2022: Subpolar Southern Ocean seasonal variability of the geostrophic circulation from multi-mission satellite altimetry. *Journal of Geophysical Research: Oceans*, e2021JC018096.

Cane, M. A., V. M. Kamenkovich, and A. Krupitsky, 1998: On the utility and disutility of JEBAR. *Journal of Physical Oceanography*, **28 (3)**, 519–526, https://doi.org/10.1175/1520-0485(1998)028⟨0519:OTUADO⟩2.0.CO;2.

Couldrey, M. P., L. Jullion, A. C. Naveira Garabato, C. Rye, L. Herráiz-Borreguero, P. J. Brown, M. P. Meredith, and K. L. Speer, 2013: Remotely induced warming of antarctic bottom water in the eastern weddell gyre. *Geophysical Research Letters*, **40 (11)**, 2755–2760.

Depoorter, M. A., J. L. Bamber, J. A. Griggs, J. T. Lenaerts, S. R. Ligtenberg, M. R. van den Broeke, and G. Moholdt, 2013: Calving fluxes and basal melt rates of Antarctic ice shelves. *Nature*, **502 (7469)**, 89–92.

Dotto, T. S., and Coauthors, 2018: Variability of the Ross Gyre, Southern Ocean: Drivers and responses revealed by satellite altimetry. *Geophysical Research Letters*, **45 (12)**, 6195–6204.

Fahrbach, E., M. Hoppema, G. Rohardt, O. Boebel, O. Klatt, and A. Wisotzki, 2011: Warming of deep and abyssal water masses along the Greenwich Meridian on decadal time scales: The Weddell gyre as a heat buffer. *Deep Sea Research Part II: Topical Studies in Oceanography*, **58 (25-26)**, 2509–2523.

Foster, T. D., and E. C. Carmack, 1976: Frontal zone mixing and Antarctic Bottom Water formation in the southern Weddell Sea. *Deep Sea Research and Oceanographic Abstracts*, Elsevier, Vol. 23, 301–317.

Golledge, N. R., D. E. Kowalewski, T. R. Naish, R. H. Levy, C. J. Fogwill, and E. G. Gasson, 2015: The multi-millennial Antarctic commitment to future sea-level rise. *Nature*, **526 (7573)**, 421–425.

Gordon, A. L., B. Huber, D. McKee, and M. Visbeck, 2010: A seasonal cycle in the export of bottom water from the Weddell Sea. *Nature Geoscience*, **3 (8)**, 551–556.

Gordon, A. L., B. A. Huber, and E. P. Abrahamsen, 2020: Interannual variability of the outflow of Weddell Sea Bottom Water. *Geophysical Research Letters*, **47 (4)**, e2020GL087 014.

Goyal, R., A. Sen Gupta, M. Jucker, and M. H. England, 2021: Historical and projected changes in the Southern Hemisphere surface westerlies. *Geophysical Research Letters*, **48 (4)**, e2020GL090 849.

Griffies, S., A. Adcroft, and R. Hallberg, 2020: A primer on the vertical Lagrangian-remap method in ocean models based on finite volume generalized vertical coordinates. *Journal of Advances in Modeling Earth Systems*, **12**, https://doi.org/10.1029/2019MS001954.

Griffies, S., and R. Hallberg, 2000: Biharmonic friction with a Smagorinsky-like viscosity for use in large-scale eddy-permitting ocean models. *Monthly Weather Review*, **128**, 2935–2946, https://doi.org/10.1175/1520-0493(2000)128⟨2935:BFWASL⟩2.0.CO;2.

Griffies, S. M., and Coauthors, 2016: OMIP contribution to CMIP6: Experimental and diagnostic protocol for the physical component of the Ocean Model Intercomparison Project. *Geoscientific Model Development*, 3231.

Grooms, I., N. Loose, R. Abernathey, J. Steinberg, S. D. Bachman, G. Marques, A. P. Guillaumin, and E. Yankovsky, 2021: Diffusion-based smoothers for spatial filtering of gridded geophysical data. *Journal of Advances in Modeling Earth Systems*, **13 (9)**, e2021MS002 552, https://doi.org/10.1029/2021MS002552.

Hallberg, R., 2013: Using a resolution function to regulate parameterizations of oceanic mesoscale eddy effects. *Ocean Modelling*, **72**, 92–103.

Hogg, A. M., and B. Gayen, 2020: Ocean gyres driven by surface buoyancy forcing. *Geophysical Research Letters*, **47 (16)**, e2020GL088 539.

Holland, W. R., 1973: Baroclinic and topographic influences on the transport in western boundary currents. *Geophysical Fluid Dynamics*, **4 (3)**, 187–210.

Hughes, C. W., 2000: A theoretical reason to expect inviscid western boundary currents in realistic oceans. *Ocean Modelling*, **2 (1-2)**, 73–83.

Hughes, C. W., and B. A. De Cuevas, 2001: Why western boundary currents in realistic oceans are inviscid: A link between form stress and bottom pressure torques. *Journal of Physical Oceanography*, **31 (10)**, 2871–2885.

Huneke, W. G., A. K. Morrison, and A. M. Hogg, 2022: Spatial and subannual variability of the Antarctic Slope Current in an eddying ocean–sea ice model. *Journal of Physical Oceanography*, **52 (3)**, 347–361.

Jullion, L., and Coauthors, 2014: The contribution of the Weddell Gyre to the lower limb of the Global Overturning Circulation. *Journal of Geophysical Research: Oceans*, **119 (6)**, 3357–3377.

Khatri, H., S. M. Griffies, B. A. Storer, M. Buzzicotti, H. Aluie, M. Sonnewald, R. Dussin, and A. E. Shao, 2023: A scale-dependent analysis of the barotropic vorticity budget in a global ocean simulation. https://doi.org/10.22541/essoar.168394747.71837050/v1, URL 10.22541/essoar.168394747.71837050/v1.

Kiss, A. E., and Coauthors, 2020: ACCESS-OM2 v1. 0: a global ocean–sea ice model at three resolutions. *Geoscientific Model Development*, **13 (2)**, 401–442.

Lago, V., and M. H. England, 2019: Projected slowdown of Antarctic Bottom Water formation in response to amplified meltwater contributions. *Journal of Climate*, **32 (19)**, 6319–6335.

Le Corre, M., J. Gula, and A.-M. Tréguier, 2020: Barotropic vorticity balance of the North Atlantic subpolar gyre in an eddy-resolving model. *Ocean Science*, **16 (2)**, 451–468.

Le Paih, N., T. Hattermann, O. Boebel, T. Kanzow, C. Lüpkes, G. Rohardt, V. Strass, and S. Herbette, 2020: Coherent seasonal acceleration of the Weddell Sea boundary current system driven by upstream winds. *Journal of Geophysical Research: Oceans*, **125 (10)**, e2020JC016 316.

Leach, H., V. Strass, and B. Cisewski, 2011: Modification by lateral mixing of the Warm Deep Water entering the Weddell Sea in the Maud Rise region. *Ocean Dynamics*, **61**, 51–68.

Li, Q., M. H. England, A. M. Hogg, S. R. Rintoul, and A. K. Morrison, 2023: Abyssal ocean overturning slowdown and warming driven by Antarctic meltwater. *Nature*, **615 (7954)**, 841–847.

Loose, N., and Coauthors, 2022: GCM-Filters: A Python package for diffusion-based spatial filtering of gridded data. *Journal of Open Source Software*, **7 (70)**, 3947, https://doi.org/10.21105/joss.03947.

McKee, D. C., X. Yuan, A. L. Gordon, B. A. Huber, and Z. Dong, 2011: Climate impact on interannual variability of Weddell Sea Bottom Water. *Journal of Geophysical Research: Oceans*, **116 (C5)**.

Meijers, A., M. Meredith, E. Abrahamsen, M. Morales Maqueda, D. Jones, and A. Naveira Garabato, 2016: Wind-driven export of Weddell Sea slope water. *Journal of Geophysical Research: Oceans*, **121 (10)**, 7530–7546.

Meredith, M. P., 2013: Replenishing the abyss. *Nature Geoscience*, **6 (3)**, 166–167.

Meredith, M. P., A. C. N. Garabato, A. L. Gordon, and G. C. Johnson, 2008: Evolution of the deep and bottom waters of the Scotia Sea, Southern Ocean, during 1995–2005. *Journal of Climate*, **21 (13)**, 3327–3343.

Meredith, M. P., A. L. Gordon, A. C. Naveira Garabato, E. P. Abrahamsen, B. A. Huber, L. Jullion, and H. J. Venables, 2011: Synchronous intensification and warming of Antarctic Bottom Water outflow from the Weddell Gyre. *Geophysical Research Letters*, **38 (3)**.

Mertz, G., and D. G. Wright, 1992: Interpretations of the JEBAR term. *Journal of Physical Oceanography*, **22 (3)**, 301–305.

Morioka, Y., and S. K. Behera, 2021: Remote and local processes controlling decadal sea ice variability in the Weddell Sea. *Journal of Geophysical Research: Oceans*, **126 (8)**, e2020JC017 036.

Morrison, A. K., W. G. Huneke, J. Neme, P. Spence, A. M. Hogg, M. H. England, and S. M. Griffies, 2023: Sensitivity of Antarctic shelf waters and abyssal overturning to local winds. *Journal of Climate*, 1–32.

Munk, W. H., 1950: On the wind-driven ocean circulation. *Journal of Atmospheric Sciences*, **7 (2)**, 80–93.

Narayanan, A., S. T. Gille, M. R. Mazloff, M. D. du Plessis, K. Murali, and F. Roquet, 2023: Zonal distribution of Circumpolar Deep Water transformation rates and its relation to heat content on Antarctic Shelves. *Journal of Geophysical Research: Oceans*, e2022JC019310.

Narayanan, A., S. T. Gille, M. R. Mazloff, and K. Murali, 2019: Water mass characteristics of the Antarctic margins and the production and seasonality of Dense Shelf Water. *Journal of Geophysical Research: Oceans*, **124 (12)**, 9277–9294.

Naveira Garabato, A., and Coauthors, 2019: Phased response of the subpolar Southern Ocean to changes in circumpolar winds. *Geophysical Research Letters*, **46 (11)**, 6024–6033.

Naveira Garabato, A., and Coauthors, 2019: Rapid mixing and exchange of deep-ocean waters in an abyssal boundary current. *Proceedings of the National Academy of Sciences*, https://doi.org/10.1073/pnas.1904087116.

Naveira Garabato, A. C., J. D. Zika, L. Jullion, P. J. Brown, P. R. Holland, M. P. Meredith, and S. Bacon, 2016: The thermodynamic balance of the Weddell Gyre. *Geophysical Research Letters*, **43 (1)**, 317–325.

Neme, J., M. H. England, and A. M. Hogg, 2021: Seasonal and interannual variability of the Weddell Gyre from a high-resolution global ocean-sea ice simulation during 1958–2018. *Journal of Geophysical Research: Oceans*, **126 (11)**, e2021JC017 662.

Neme, J., M. H. England, and A. McC. Hogg, 2022: Projected changes of surface winds over the Antarctic continental margin. *Geophysical Research Letters*, **49 (16)**, e2022GL098 820.

Newsom, E. R., C. M. Bitz, F. O. Bryan, R. Abernathey, and P. R. Gent, 2016: Southern Ocean deep circulation and heat uptake in a high-resolution climate model. *Journal of Climate*, **29 (7)**, 2597–2619.

Nicholls, K. W., S. Østerhus, K. Makinson, T. Gammelsrød, and E. Fahrbach, 2009: Ice-ocean processes over the continental shelf of the southern Weddell Sea, Antarctica: A review. *Reviews of Geophysics*, **47 (3)**.

Purkey, S. G., W. M. Smethie Jr, G. Gebbie, A. L. Gordon, R. E. Sonnerup, M. J. Warner, and J. L. Bullister, 2018: A synoptic view of the ventilation and circulation of Antarctic Bottom Water from chlorofluorocarbons and natural tracers. *Annu. Rev. Mar. Sci*, **10**, 503–527.

Reeve, K. A., O. Boebel, V. Strass, T. Kanzow, and R. Gerdes, 2019: Horizontal circulation and volume transports in the Weddell Gyre derived from Argo float data. *Progress in Oceanography*, **175**, 263–283.

Ryan, S., M. Schröder, O. Huhn, and R. Timmermann, 2016: On the warm inflow at the eastern boundary of the Weddell Gyre. *Deep Sea Research Part I: Oceanographic Research Papers*, **107**, 70–81.

Schoonover, J., and Coauthors, 2016: North Atlantic barotropic vorticity balances in numerical models. *Journal of Physical Oceanography*, **46 (1)**, 289–303.

Solodoch, A., A. Stewart, A. M. Hogg, A. Morrison, A. Kiss, A. Thompson, S. Purkey, and L. Cimoli, 2022: How does Antarctic Bottom Water cross the Southern Ocean? *Geophysical Research Letters*, **49 (7)**, e2021GL097 211.

Sonnewald, M., K. Reeve, and R. Lguensat, 2023: A Southern Ocean supergyre as a unifying dynamical framework identified by physics-informed machine learning. *Communications Earth & Environment*, **4**, https://doi.org/10.1038/s43247-023-00793-7.

Sonnewald, M., C. Wunsch, and P. Heimbach, 2019: Unsupervised learning reveals geography of global ocean dynamical regions. *Earth and Space Science*, **6 (5)**, 784–794.

Stewart, A. L., J. C. McWilliams, and A. Solodoch, 2021: On the role of bottom pressure torques in wind-driven gyres. *Journal of Physical Oceanography*, **51 (5)**, 1441–1464.

Stewart, A. L., and A. F. Thompson, 2015: Eddy-mediated transport of warm Circumpolar Deep Water across the Antarctic shelf break. *Geophysical Research Letters*, **42 (2)**, 432–440.

Stewart, A. L., and A. F. Thompson, 2016: Eddy generation and jet formation via dense water outflows across the Antarctic continental slope. *Journal of Physical Oceanography*, **46 (12)**, 3729–3750.

Stewart, K. D., and Coauthors, 2020: JRA55-do-based repeat year forcing datasets for driving ocean–sea-ice models. *Ocean Model.*, **147**, 101 557.

Stommel, H., 1948: The westward intensification of wind-driven ocean currents. *Eos, Transactions American Geophysical Union*, **29 (2)**, 202–206.

Styles, A. F., M. J. Bell, D. P. Marshall, and D. Storkey, 2022: Spurious forces can dominate the vorticity budget of ocean gyres on the C-grid. *Journal of Advances in Modeling Earth Systems*, **14 (5)**, e2021MS002 884.

Sverdrup, H. U., 1947: Wind-driven currents in a baroclinic ocean; with application to the equatorial currents of the eastern Pacific. *Proceedings of the National Academy of Sciences*, **33 (11)**, 318–326.

Thompson, A. F., A. L. Stewart, P. Spence, and K. J. Heywood, 2018: The Antarctic Slope Current in a changing climate. *Reviews of Geophysics*, **56 (4)**, 741–770.

Tsujino, H., and Coauthors, 2018: JRA-55 based surface dataset for driving ocean–sea-ice models (JRA55-do). *Ocean Modelling*, **130**, 79–139.

Vernet, M., and Coauthors, 2019: The Weddell Gyre, Southern Ocean: present knowledge and future challenges. *Reviews of Geophysics*, **57 (3)**, 623–708.

Waldman, R., and H. Giordani, 2023: Ocean barotropic vorticity balances: theory and application to numerical models. *Journal of Advances in Modeling Earth Systems*, **15 (4)**, e2022MS003 276, https://doi.org/10.1029/2022MS003276.

Wang, Z., and M. Meredith, 2008: Density-driven Southern Hemisphere subpolar gyres in coupled climate models. *Geophysical Research Letters*, **35 (14)**.

Wilson, E. A., A. F. Thompson, A. L. Stewart, and S. Sun, 2022: Bathymetric control of subpolar gyres and the overturning circulation in the Southern Ocean. *Journal of Physical Oceanography*, **52 (2)**, 205–223.

Yeager, S., 2015: Topographic coupling of the Atlantic overturning and gyre circulations. *Journal of Physical Oceanography*, **45 (5)**, 1258–1284.

Zhou, L., C. Heuzé, and M. Mohrmann, 2022: Early winter triggering of the Maud Rise polynya. *Geophysical Research Letters*, **49 (2)**, e2021GL096 246.

Zhou, S., A. J. Meijers, M. P. Meredith, E. P. Abrahamsen, P. R. Holland, A. Silvano, J.-B. Sallée, and S. Østerhus, 2023: Slowdown of Antarctic Bottom Water export driven by climatic wind and sea-ice changes. *Nature Climate Change*, 1–9.